ACS POLYMERS Au
AN OPEN ACCESS JOURNAL OF THE AMERICAN CHEMICAL SOCIETY

pubs.acs.org/polymerau
Article

Exploring the Role of Hydroxy- and Phosphate-Terminated *cis*-1,4-Polyisoprene Chains in the Formation of Physical Junction Points in Natural Rubber: Insights from Molecular Dynamics Simulations

Mayank Dixit* and Takashi Taniguchi*

Cite This: *ACS Polym. Au* 2024, 4, 273−288
Read Online

ACCESS | Metrics & More | Article Recommendations | Supporting Information

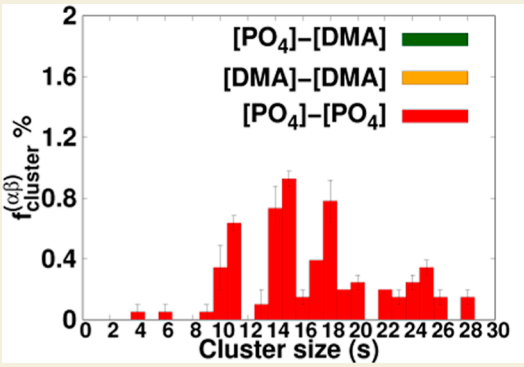

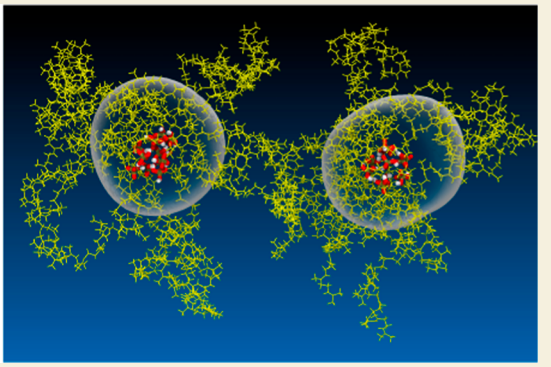

ABSTRACT: This study elucidates the pivotal role of terminal structures in *cis*-1,4-polyisoprene (PI) chains, contributing to the exceptional mechanical properties of Hevea natural rubber (NR). NR's unique networking structure, crucial for crack resistance, elasticity, and strain-induced crystallization, involves two terminal groups, ω and α. The proposed ω terminal structure is dimethyl allyl-(*trans*-1,4-isoprene)$_2$, and α terminals exist in various forms, including hydroxy, ester, and phosphate groups. Among others, we investigated three types of *cis*-1,4-PI with different terminal combinations: $_H$PI$_H$ (pure PI with H terminal), $_\omega$PI$_{\alpha 6}$ (PI with ω and α6 terminals), and $_\omega$PI$_{PO_4}$ (PI with ω and PO_4 terminals) and revealed significant dynamics variations. Hydrogen bonds between α6 and α6 and PO_4 and PO_4 residues in $_\omega$PI$_{\alpha 6}$ and $_\omega$PI$_{PO_4}$ systems induce slower dynamics of hydroxy- and phosphate-terminated PI chains. Associations between α6 and α6 and PO_4 and PO_4 terminals are markedly stronger than ω and ω, and hydrogen terminals in $_H$PI$_H$ and $_\omega$PI$_{\alpha 6,PO_4}$ systems. Phosphate terminals exhibit a stronger mutual association than hydroxy terminals. Potentials of mean force analysis and cluster-formation-fraction computations reveal stable clusters in $_\omega$PI$_{\alpha 6}$ and $_\omega$PI$_{PO_4}$, supporting the formation of polar aggregates (physical junction points). Notably, phosphate terminal groups facilitate large and highly stable phosphate polar aggregates, crucial for the natural networking structure responsible for NR's outstanding mechanical properties compared to synthetic PI rubber. This comprehensive investigation provides valuable insights into the role of terminal groups in *cis*-1,4-PI melt systems and their profound impact on the mechanical properties of NR.

KEYWORDS: *phosphate terminal group, large size cluster, potentials of mean force, hydrogen bond, polar aggregates*

1. INTRODUCTION

The unique networking structure in natural rubber (NR) imparts superior chemical and mechanical properties compared to synthetic *cis*-1,4-polyisoprene rubber (PI).[1−12] Although synthetic PI rubber has been adopted as an alternative due to limited NR production, its comprehensive properties still lag behind NR.[13] The exceptional properties of NR over PI rubber arise from the natural networking structure formed between nonrubber components and the terminal groups of *cis*-1,4-PI chains.[3,11,12] Therefore, elucidating the role of terminal groups in NR can provide valuable insights for designing new rubber materials. Hevea NR consists of rubber particles, protein, lipids, carbohydrates, metal ions, and other components.[2,14−19] The main constituents of Hevea NR are *cis*-1,4-PI and two types of terminal groups.[2,14,15,20,21] These terminal groups are referred to as ω-terminal and α-terminal. The ω-terminal consists of a dimethylallyl group and 2−3 trans isoprene. The α-terminals are considered to be categorized into those containing hydroxy,

Received: March 14, 2024
Revised: April 23, 2024
Accepted: April 23, 2024
Published: May 15, 2024

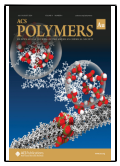

https://doi.org/10.1021/acspolymersau.4c00019
ACS Polym. Au 2024, 4, 273−288

Table 1. Details of the Three Melt Systems, $_{H}PI_{H}$, $_{\omega}PI_{\alpha 6}$, and $_{\omega}PI_{PO_4}$[a]

system code	terminal-1	*Cis*-isoprene	terminal-2	*N*	*M*	*NVT* ns	simulated annealing ns	*NPT* ns	*NVT* production run ns
PI_0 ($_{H}PI_{H}$)	H-terminal	24	H-terminal	24	512	20	20	100	1000
PI_{VI} ($_{\omega}PI_{\alpha 6}$)	ω	21	Hydroxy-terminated *cis*-1,4-isoprene ($\alpha 6$)	24	512	20	20	100	1000
PI_{ph} ($_{\omega}PI_{PO_4}$)	ω	21	Phosphate-terminated *cis*-1,4-isoprene	24	512	20	20	100	5000

[a]*N* is the number of monomers in each polymer chain and *M* is the number of chains present in each melt system. The full-atom MD simulations were performed in the sequence, i.e., *NVT* → simulated-annealing → *NPT*-EQ → *NVT*-production-run.

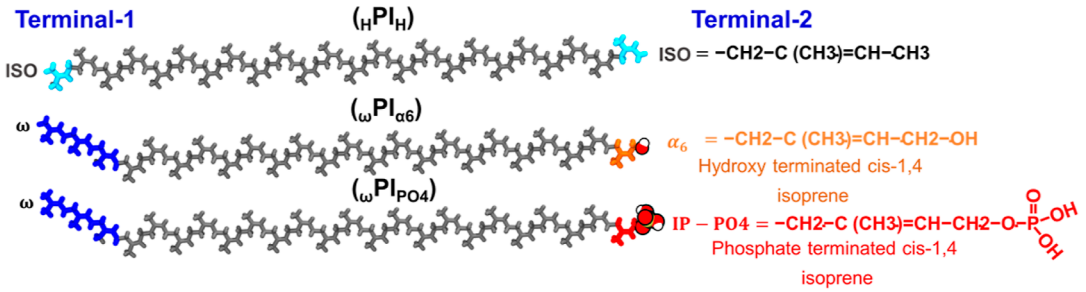

Figure 1. Extended structure of the *cis*-1,4-polyisoprene (PI) chain of pure PI terminated by H ($_{H}PI_{H}$), $_{\omega}PI_{\alpha 6}$, and $_{\omega}PI_{PO_4}$. End-isoprene residues of pure PI are shown by the cyan color. ω-Terminals (dimethyl allyl group and two *trans*-1,4-isoprene) are shown by blue color, $\alpha 6$ terminal is shown by orange color, and PO_4 is shown by red color. Backbone carbon and hydrogen atoms are shown in gray color and the oxygen and hydrogen atoms of −OH are shown in red and white colors, respectively.

ester, and phosphate groups.[1,3,16,20−25] Previous investigations have conducted structural analysis using solution NMR on the terminal units of NR subsequent to chemical treatment involving alterations such as deproteinization with enzymes and other chemicals.[2,26,27] These studies revealed the presence of monophosphate, diphosphate, and phospholipids at the α-terminus.[2,26−28] In contrast, Oouchi et al. devised a NMR-based approach to analyze terminal unit structures in commercial NR, either without chemical treatments or with mild treatments like acetone extraction to remove impurities. Their novel methods, integrating 2D-NMR, effectively suppressed signals from low-molecular-weight impurities. Employing these techniques, they detected NMR signals of terminal units in chemically untreated NR. Analysis of eight commercial H-NR samples consistently revealed six α-terminus terminating-end units, with none forming a phosphate ester.[1] Hence, there is a contradiction between these two experimental research studies. This disparity between experimental findings necessitates a thorough investigation into the molecular characteristics of these α-terminal groups in NR. It is also reported in the literature[2,3,24,29] that, in a melt of natural *cis*-1,4-PI, a physical network structure is formed through hydrogen bonds (HBs) in α-terminal and through hydrogen and ionic bonds with phospholipids, while ω-terminal bonds are formed with protein molecules. These branch points in the network play a vital role in polymer chain elongation during deformation. Previous research utilizing NMR has suggested that lipid molecules form physical junction points with α-terminal through hydrogen and ionic bonds.[2,14,15,22,23,25] Recent experimental studies have also indicated the significance of physical junction points by terminal groups in the strain-induced crystallization (SIC) of NR.[18,30−32] Moreover, a synthesized phosphate-terminated PI rubber has shown improved mechanical properties compared to pure PI rubber due to multiple physical junction points mediated by phosphate terminal groups.[33] Recent findings demonstrate that phosphorylcholine groups function as cross-linking sites (physical junction points) in both unvulcanized and vulcanized rubber, thereby enhancing mechanical characteristics through the facilitation of SIC. Conversely, polymers featuring pendant hydroxyl groups exhibit sequence-specific SIC behaviors attributed to their nonaggregating nature.[34] However, the structural mechanism of physical junction point formation remains unclear. To address this knowledge gap, we perform coarse-grained and all-atom molecular dynamics (MD) simulations, investigating the role of ω-terminal and two types of α'-terminals (i.e., $\alpha 6$-terminal group and IP−PO_4 terminal group) in the formation of physical junction points by PI chains. In this work, we used the terminology α'-terminal instead of α-terminal because the terminal-containing PO_4 has not been confirmed yet by an experiment to be a terminal group of *cis*-1,4-PI taken from a rubber tree. Our multiscale approach is based on our recent work,[22−25] where we developed a model for *cis*-1,4-PI chains with six types of terminal groups (i.e., from $\alpha 1$ to $\alpha 6$, according to their notation).[1] The $\alpha 6$-terminal group represents hydroxy-terminated 1,4-cis-isoprene [$-CH_2-C(CH_3)=CH-CH_2-OH$] and IP−PO_4] terminal group represents phosphate-terminated 1,4-cis-isoprene [$-CH_2-C(CH_3)=CH-CH_2-H_2PO_4$]. Therefore, there is structural similarity of monomer units in between $\alpha 6$ and IP−PO_4 terminal groups. Henceforth, the notation for the $-H_2PO_4$ group shall be simplified to $-PO_4$. Table 1 provides details of the three distinct melt systems with different terminal groups (see Figure 1). Molecular modeling and MD simulations have been invaluable in investigating the mechanical and chemical properties of polymers, complementing experimental studies.[24,35−62] In our recent research,[22−25] we employed a multiscale approach to explore the interactions of terminal groups in the *cis*-1,4-PI chain, which was recently generated as reported by Choi et al.[63] In the current study, we focus on *cis*-1,4-PI with ω-terminal and two distinct types of α' terminals, namely, the $\alpha 6$-terminal group and the PO_4 terminal group. In addition, as a reference melt system, we also consider a melt system of hydrogen-terminated *cis*-1,4-PI ($_{H}PI_{H}$). Namely, we investigate three different melt systems ($_{H}PI_{H}$), $_{\omega}PI_{\alpha 6}$, and $_{\omega}PI_{PO_4}$, each characterized by unique combinations of ω-

https://doi.org/10.1021/acspolymersau.4c00019
ACS Polym. Au 2024, 4, 273−288

terminal and α'-terminal groups (illustrated in Figure 1). Our approach builds upon the same multiscale model utilized in our previous work.[22−25] Detailed information about each melt system is provided in Table 1.

2. METHODOLOGY AND COMPUTATIONAL DISCRIPTIONS

In this investigation, we explore three distinct types of *cis*-1,4-PI melt systems, each characterized by different combinations of ω-terminal and α'-terminal groups (details are provided in Table 1 and Figure 1). To ensure sufficient statistical sampling, we include 512 *cis*-1,4-PI chains in each melt system, with each chain comprising 24 monomers (M = 512 and N = 24). This approach aligns with our previous work, where we also considered a similar combination but solely focused on the six types of α-terminals.[22−25] Experimental studies have revealed that NRs with low molecular weights exhibit enhanced mechanical and rheological properties, owing to a high density of terminal groups.[64−66] These terminal groups readily associate, potentially interacting with nonrubber components such as proteins, lipids, and sugars, thereby facilitating the formation of the natural network structure.[66] In contrast, NRs with longer polymer chains exhibit poorer mechanical and physical properties due to the formation of a lower fraction of chain end group aggregates. Hence, we have chosen short PI chains in this study to gain molecular-level insights into terminal group aggregates. The molecular weight range of natural PI obtained from rubber trees spans from 100 kDa to 2000 kDa,[67,68] which is considerably large and too lengthy to be efficiently handled in numerical simulations. The primary objective of this study is to elucidate the difference in the formation of physical junction points among these terminals in the three types of polymer melt systems. Thus, we consider a *cis*-1,4-PI chain with a molecular weight of 1.6 kDa, which provides an adequate length for achieving the goals of this investigation.

2.1. All-Atom Molecular Dynamics Protocol

The initial configuration of each melt system is generated through a multiscale approach, as detailed in our previous publications.[22−25] These initial structures (refer to Figure S1) are utilized as starting points for all-atom MD simulations, employing GROMACS version-2019.2.[69] The CHARMM general all-atom force field,[70,71] extensively validated for various polymer melt systems,[63] is employed for these simulations. The temperature and pressure are set to 360 K and 1 bar, respectively, following similar conditions from our previous work.[22,24,25] To prepare the systems, the initial structures are energy-minimized, and subsequently, *NVT* equilibration, *NPT* simulated annealing, and *NPT* equilibrations are performed (see Table 1 for the respective classical MD simulation times for each step). The equilibrated structure is then subjected to a production run spanning 1000−5000 ns. The trajectories generated from these simulations enable the computation of the radius of gyration, end-to-end distance, and radial distribution function between terminal groups, thereby elucidating the local structure of branching physical junction points between or among PI chain ends. To maintain the system temperature, we employ the Nosé−Hoover thermostat with a coupling constant of 1 ps. The system pressure is controlled at 1 bar using both the Berendsen barostat and Parrinello−Rahman barostat[72] during equilibration and the production run, with time constants of 5 ps and a compressibility of 4.5×10^{-5} bar^{-1} (4.5×10^{-10} Pa^{-1}), respectively. The Verlet cutoff scheme is employed to build the neighbor list, with a cutoff radius of 1.2 nm for all-atom MD simulations. The LINCS algorithm[73] is utilized to constrain HB lengths. A time step of 2 fs is employed for all-atom MD, while the particle mesh Ewald method[74] is employed for calculating electrostatic interactions.

3. RESULTS

3.1. Equilibration of Polyisoprene Chains

In this section, we expound upon the outcomes derived from our all-atom MD simulations. The subject of our investigation revolves around the intricate assessment of static and dynamic properties, encompassing end-to-end distances, radii of gyration, as well as mean square internal distance and end-to-end vector autocorrelation functions, and Rouse mode analysis in relation to PI chains featured in the three distinct systems, as detailed in Table 1.

Through a systematic exploration, we scrutinized the equilibrium properties of PI chains, delving into key parameters such as the end-to-end distance (R_{ee}), radius of gyration (R_g), and mean square internal distances $\langle R^2(n)\rangle$. Capturing the temporal evolution of the end-to-end distance and radius of gyration via Figure S2 (provided in the Supporting Information), we observed remarkable stability over the course of the production run, signifying the establishment of equilibrium within the polymer chains across all PI melt systems. Moreover, we conducted a thorough evaluation, calculating the mean square end-to-end distance $\langle R_{ee}^2\rangle$ and the mean square radius of gyration $\langle R_g^2\rangle$, and the ensuing ratio $\langle R_{ee}^2\rangle/\langle R_g^2\rangle$ is documented in Table 2. Our observations, encapsulated in Table 2, demonstrate

Table 2. Mean-Square End-to-End Distance, $\langle R_{ee}^2\rangle$, Mean Square Radius of Gyration, $\langle R_g^2\rangle$, Kuhn Length, b, and Number of Kuhn Segments, N_{RB}, for all Melt Systems at 360 K and 1 bar

system	$\langle R_{ee}^2\rangle$ [nm^2]	$\langle R_g^2\rangle$ [nm^2]	$\langle R_{ee}^2\rangle/\langle R_g^2\rangle$	b [nm]	N_{RB}
$_{H}PI_{H}$	8.73 ± 0.25	1.43 ± 0.02	6.11	0.80	13.50
$_{\omega}PI_{\alpha 6}$	9.00 ± 0.30	1.44 ± 0.03	6.23	0.81	13.59
$_{\omega}PI_{PO_4}$	10.72 ± 0.15	1.61 ± 0.01	6.64	0.94	11.3

the close adherence to a Gaussian behavior for the PI chains. The Kuhn length b characterizing a polymer is precisely defined as the quotient of the mean square end-to-end distance $\langle R_{ee}^2\rangle$ and the maximum size when the polymer chain is fully extended R_{max}

$$b = \frac{\langle R_{ee}^2\rangle}{R_{max}}$$
$$R_{max} = bN_{RB} \quad (1)$$

The variables b, representing the Kuhn length of the polymer chain, N_{RB}, denoting the number of Kuhn segments, and R_{max}, indicating the fully extended length of the polymer chain. Our investigation has involved the estimation of both the Kuhn length and the number of Kuhn segments for the polymer chain within each melt system, with detailed results presented in Table 2. The derived values for the Kuhn lengths exhibit close alignment with experimental data.[75]

The investigation of chain conformations in each melt system was duly characterized through the utilization of mean square internal distances $\langle R^2(n)\rangle$, as elucidated by Figure S3 (contained in the Supporting Information). By averaging these quantities over all segments of size $n = i - j$ along the chains, where $i < j \in$

https://doi.org/10.1021/acspolymersau.4c00019
ACS Polym. Au 2024, 4, 273−288

$[1, N]$ denotes monomer indices, we acquired profound insights into the overall system behavior. Notably, our findings underscore the sufficiency of the simulation duration for each melt system, as the chains exhibited extensive movement, spanning multiple times their individual dimensions.

The computation of the end-to-end vector autocorrelation function, denoted as $C(t)$, was executed as an essential aspect of our investigation. This correlation function was assessed as a function of simulation time for each distinct melt system, employing the following well-established equation

$$C(t) = \langle \frac{\mathbf{R}(t)\cdot\mathbf{R}(0)}{\mathbf{R}(0)\cdot\mathbf{R}(0)} \rangle \quad (2)$$

Herein, $\mathbf{R}(0)$ and $\mathbf{R}(t)$ represent the end-to-end vectors at time t = 0 and time t, respectively, and the angle bracket signifies an ensemble average. The graphical depiction of $C(t)$ for the three distinct systems (PI_0, PI_{VI}, and PI_{ph}) is presented in Figure 2.

(a) The rotational relaxation behavior of a PI chain in the three melt systems $PI_{0,VI,ph}$

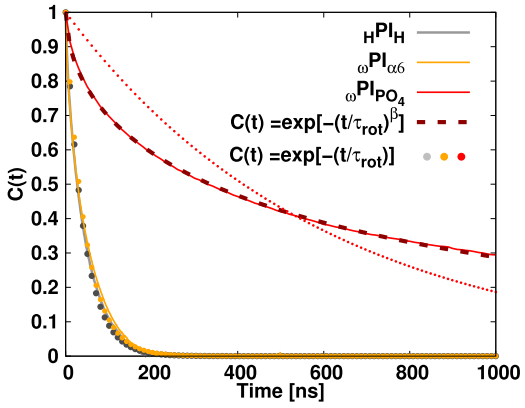

(b) The rotational relaxation time τ_{rot} of polymer chains for each melt system.

Systems	Relaxation time τ_{rot} [ns] $(\beta = 1)$	Relaxation time τ_{rot} [ns] $(\beta \neq 1)$
$_H$PI$_H$	45.41±0.01	42.50±0.01 $(\beta = 0.88)$
$_\omega$PI$_{\alpha 6}$	57.23±0.01	49.05±0.01 $(\beta = 0.97)$
$_\omega$PI$_{PO_4}$	804.04 ± 0.58	574.24±0.25 $(\beta = 0.46)$

Figure 2. Rotational correlation functions as a function of time for each melt system. In panel (a), the dashed lines represent fits to the stretched exponential function, $C(t) = \exp[-(t/\tau_{rot})^{\beta}]$, on the other hand, the solid circle stands for a fit to a simple exponential function, $C(t) = \exp[-(t/\tau_{rot})]$. Panel (b) showcases the corresponding rotational relaxation times, denoted as τ_{rot}. Computation of τ_{rot} is achieved by fitting the end-to-end vector autocorrelation functions, $C(t)$, to a simple exponential function and stretched exponential function.

Additionally, we undertook an estimation of the average rotational relaxation time, achieved through a fitting procedure of the time correlation function to the simple exponential function as well as the stretched exponential function,[76] which is defined below

$$C(t) = \exp\left[-\left(\frac{t}{\tau_{rot}}\right)^{\beta}\right] \quad (3)$$

The rotational relaxation times, denoted as τ_{rot}, and the associated stretching exponents, represented as β for the three distinct systems, are illustrated in Figure 2b. In the case of the simple exponential function, β = 1 while for the stretched exponential function, β < 1. As seen from Figure 2a, the data for $_H$PI$_H$ and $_\omega$PI$_{\alpha 6}$ are well fitted by the simple exponential function, but for $_\omega$PI$_{PO_4}$, the stretched exponential function gave a better fit. Intriguingly, the observed order of relaxation times exhibits a distinct hierarchy: $_H$PI$_H$ < $_\omega$PI$_{\alpha 6}$ ≪ $_\omega$PI$_{PO_4}$. From the analysis of Figure 2b, we can see that the rotational relaxation times computed by using stretched exponential functions are always, respectively, smaller than the ones computed by using simple exponential decay functions. This compelling finding emphasizes that the presence of hydroxy and phosphate terminal groups significantly retards the dynamics of PI chains when compared to hydrogen-terminated PI chains. Especially the phosphate terminal groups alter the fashion of relaxation dynamics to the stretched exponential decay (β = 0.46) from a simple exponential decay one. In addition, in the $_\omega$PI$_{PO_4}$ melt, the substantially long relaxation time τ_{rot}, (i.e., ten times or more, longer than the other two systems) is observed.

3.2. Rouse Mode Analysis

We conduct Rouse mode analysis on the all-atom chains, which are represented as coarse-grained chains comprising 12 Rouse beads based on the data, as shown in Table 2. In accordance with the Rouse model,[77] the normal coordinate is evaluated as $\mathbf{X}_p$ for free chain ends is defined as

$$\boldsymbol{X}_p(t) = \sum_{j=1}^{N_{RB}} \sqrt{\frac{2}{N_{RB}}} \cos\left(\frac{(j-1/2)p\pi}{N_{RB}}\right) \boldsymbol{r}_j(t) \quad (4)$$

Here, N_{RB} denotes the count of Rouse beads within a chain, while $\mathbf{r}_j$ denotes the position of the j-th Rouse bead.[78−81] In the context of a Rouse chain with free ends, the theoretical expectation dictates the relationship $\tau_p/\tau_R = 1/p^2$. Here, $\tau_R(\equiv\tau_1)$ is the longest chain relaxation time.

The Rouse mode analysis for a polymer chain with fully immobilized chain ends can be conducted through the utilization of the subsequent normal coordinate[82]

$$\boldsymbol{X}_p(t) = \frac{1}{N_{RB}} \int_0^{N_{RB}} \sin\left(\frac{(p-1/2)n\pi}{N_{RB}}\right) \boldsymbol{r}_n(t)\mathrm{d}n \quad (5)$$

Under the condition of fixed chain ends, the anticipated theoretical relationship is expressed as $\tau_p/\tau_R = 1/(p-1/2)^2$.

We computed the time autocorrelation function $\langle \mathbf{X}_p(t)\cdot\mathbf{X}_p(0)\rangle/\langle \mathbf{X}_p(0)\cdot\mathbf{X}_p(0)\rangle$ for various Rouse modes, namely, p = 1, 2, 3, 4, 5, and 6, derived from the current all-atom MD simulations. The corresponding time autocorrelation functions are illustrated in Figure S4 of the Supporting Information. In Table 3, the longest chain relaxation time τ_1 corresponding to the first Rouse mode (p = 1), is depicted for every melt system. In Figure 2b, τ_{rot}, obtained through fitting a simple exponential decay function to the rotational correlation function $C(t)$ for each melt system, is also presented. A consistent pattern is noted between the chain relaxation time of the first Rouse mode τ_1 (see Table 3) and the rotational relaxation time τ_{rot}. (Figure 2b).

Table 3. Chain Relaxation Time τ_p for First Rouse Mode (p = 1)[a]

systems	type of alpha terminal	τ_R [ns]	τ_R (system)/τ_R ($_H$PI$_H$)
$_H$PI$_H$		48.88 ± 0.01	1.00
$_\omega$PI$_{\alpha 6}$	hydroxy	57.07 ± 0.01	1.17
$_\omega$PI$_{PO_4}$	phosphate	750.05 ± 0.25	15.34

[a]The fitting of the time autocorrelation function $\langle \mathbf{X}_p(t)\cdot\mathbf{X}_p(0)\rangle/\langle \mathbf{X}_p(0)\cdot\mathbf{X}_p(0)\rangle$ with a simple exponential function for extracting the chain relaxation time τ_p.

https://doi.org/10.1021/acspolymersau.4c00019
ACS Polym. Au 2024, 4, 273−288

Consistent with the predictions of the Rouse theory,[77] the envisaged scaling behavior of relaxation times τ_p corresponds to each normal mode p is expounded. The theoretical framework asserts that in the absence of constrained chain-ends, the scaling relationship is expressed as $\tau_p/\tau_R = 1/p^2$, while under fixed chain-ends, the relationship transforms to $\tau_p/\tau_R = 1/(p - 1/2)^2$.[82] Figure 3 visually illustrates the dependence of the τ_p on the

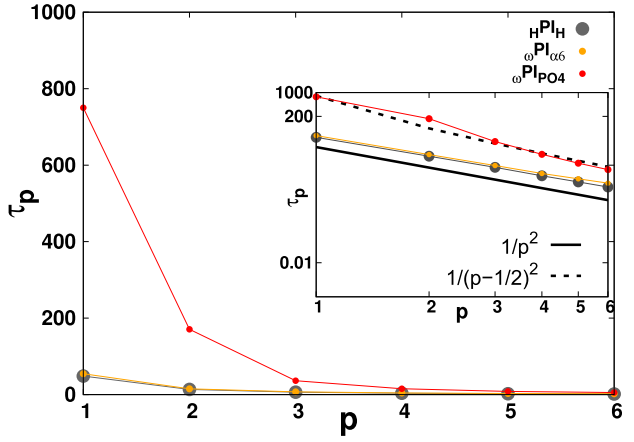

Figure 3. Plot of τ_p vs p. Figure illustrates the relaxation times corresponding to distinct normal modes p of the polymer chains, elucidating the dynamic characteristics of the melt system. In the inset of the plot, we have shown the log−log plot of τ_p-vs-p.

normal mode p. The determination of relaxation times τ_p for polymer chains in each melt system involves fitting the time autocorrelation function $\langle \mathbf{X}_p(t)\cdot\mathbf{X}_p(0)\rangle/\langle \mathbf{X}_p(0)\cdot\mathbf{X}_p(0)\rangle$ with a simple exponential function, namely, $\exp(-t/\tau_p)$. If Rouse scaling is valid, all curves presented in Figure 3 are anticipated to converge onto a unified trajectory, reflecting $\tau_p/\tau_R = 1/p^2$ for unconfined chain-ends and $\tau_p/\tau_R = 1/(p - 1/2)^2$ for fixed chain-ends. In the case of PI_0 ($_HPI_H$), where PI chains possess free chain-ends, adherence to Rouse scaling is evident (indicated by the gray color symbol ● in Figure 3 for Rouse modes p = 1, 2, 3, 4, 5, and 6). Likewise, for the $_\omega PI_{\alpha 6}$ melt system, the PI chains also adhere to free-end Rouse scaling, suggesting that any deviation in higher modes is not triggered by intermittent associations among chain ends. In Table 3, we present the chain relaxation time τ_R for each molten system under consideration.

The observations from Figure 3 and Table 3 collectively suggest that the system $_\omega PI_{\alpha 6}$, characterized by end-group associations, maintains adherence to the scaling principles of the Rouse model with free ends. However, it manifests a prolonged relaxation time scale due to the intermittently constrained dynamics of chain ends. Conversely, the $_\omega PI_{PO_4}$ melt system conforms similar behavior to $1/(p - 1/2)^2$. In addition, from Table 3, we can see that the relaxation time can be substantially enhanced by PO_4 groups. Based on the findings of the current analyses, the intermittent interaction among $\alpha 6$-terminals does not alter the Rouse dynamics behavior; however, it does modulate the time scale of Rouse relaxation. Conversely, the association among PO_4 groups results in deviation from the behavior of a Rouse chain with free chain-ends, particularly for first and second Rouse modes (p = 1 and 2), and significantly augments the relaxation time of $_\omega PI_{PO_4}$ chains.

3.3. Structure Aggregates of Hydroxylated- and Phosphorylated *cis*-1,4-Polyisoprene Chains

In this section, our focus centers on the examination of associations between terminal groups, specifically ISO−ISO, $\omega-\omega$, $\alpha 6-\alpha 6$, and PO_4-PO_4, in the PI_0, PI_{VI}, and PI_{ph} melt systems. Figure 4 presents snapshots of the PI_0, PI_{VI}, and PI_{ph}

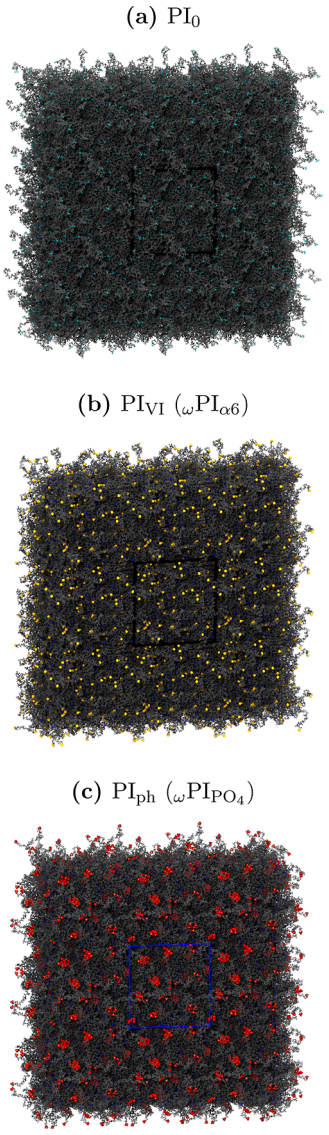

Figure 4. Snapshots of the (a) PI_0, (b) PI_{VI}, and (c) PI_{ph} melt systems captured after the final production-run of all-atom MD simulations. ω terminals are represented by the dimethyl allyl group (shown in blue), along with two *trans*-1,4-isoprene moieties. $\alpha 6$ and PO_4 terminals are depicted in orange and red colors, respectively, while the *cis*-1,4-isoprene units are represented in cyan. The backbone carbon and hydrogen atoms of each primary PI chain are illustrated in gray color, providing a comprehensive view of the molecular arrangement within the systems.

melt systems after the production run. Remarkably, we observed distinct characteristics in the aggregate states of $\alpha 6-\alpha 6$ and PO_4-PO_4, clearly evident in the snapshots, while such an aggregate state is notably absent for ISO−ISO.

In order to gain insight into the local structural organization of terminal groups surrounding a specific terminal group, we have conducted a thorough investigation using radial distribution

https://doi.org/10.1021/acspolymersau.4c00019
ACS Polym. Au 2024, 4, 273−288

functions (RDFs). These RDFs, denoted as $g_{\alpha\beta}(r)$, are estimated by assessing the distribution of distances between the centers of mass of various *cis*-1,4-PI chains' terminal groups. The RDFs are mathematically described by the following equation

$$g_{\alpha\beta}(r) = \frac{\langle \rho_\beta(r)\rangle_{\text{local},\alpha}}{\langle \rho_\beta(r_c)\rangle_\alpha} \tag{6}$$

The expression for $\langle \rho_\beta(r)\rangle_{\text{local},\alpha}$ represents the average density of type β particles in the vicinity of type α particles at a given distance r. This density is calculated as follows

$$\langle \rho_\beta(r)\rangle_{\text{local},\alpha} = \frac{1}{N_\alpha(\delta_{\alpha\beta}+1)} \sum_{i_\alpha=1}^{N_\alpha} \langle \rho_\beta(r)\rangle_{\text{local},i_\alpha} \tag{7}$$

In eq 7, $\langle \rho_\beta(r)\rangle_{\text{local},i_\alpha}$ represents the local density of type β particles surrounding the i-th type α particle at a specific distance r. This local density is defined as follows

$$\langle \rho_\beta(r)\rangle_{\text{local},i_\alpha} = \sum_{j_\beta=1}^{N_\beta}{}' \delta(r_{i_\alpha j_\beta} - r) \tag{8}$$

In eq 8, the primed summation notation introduces a distinction based on the relationship between α and β. Specifically, when α and β represent different particle types, the summation, denoted as $\sum'$, spans from $j_\beta = 1$ to N_β. Conversely, when α and β refer to the same particle type, the summation, represented as $\sum'$, excludes the contribution from the i_α-th particle and extends from $j_\beta = 1$ to N_β, with the exclusion of $j_\beta \neq i_\alpha$. The denominator on the right-hand side of eq 6, $\langle \rho_\beta(r_c)\rangle_\alpha$, characterizes the average density of particle type β within a sphere of radius r_c, which is centered around the α particle. It is mathematically defined as follows

$$\langle \rho_\beta(r_c)\rangle_\alpha = \frac{1}{N_\alpha} \sum_{i_\alpha=1}^{N_\alpha} \langle \rho_\beta(r_c)\rangle_{i_\alpha} \tag{9}$$

where $\langle \rho_\beta(r_c)\rangle_{i\alpha}$ designates the density of particle type β confined within a sphere of radius r_c, centered around the i-th type α particle. This quantity is defined as follows

$$\langle \rho_\beta(r_c)\rangle_{i_\alpha} = \frac{1}{V}\int_0^{r_c} \langle \rho_\beta(r)\rangle_{\text{local},i_\alpha} 4\pi r^2 \mathrm{d}r \tag{10}$$

where V denotes the volume of the sphere, and the value of r_c is set to half of the box length. N_α represents the total number of α particles. Additionally, the Kronecker delta, $\delta_{\alpha\beta}$, takes the values of 1 if $\alpha = \beta$, and 0 if $\alpha \neq \beta$. To avoid double counting in the case $\alpha = \beta$, the factor $(\delta_{\alpha\beta} + 1)$ is introduced in the denominator. In this context, our focus lies in the investigation of the solvation structure of terminal groups around a specific terminal group. This exploration offers valuable insights into the local molecular interactions and spatial arrangement of the terminal groups in the system under study. In the course of this investigation, a comprehensive analysis has been carried out to examine the RDFs pertaining to several key molecular components. Specifically, we have scrutinized the RDFs involving the center of mass of the dimethyl allyl ([DMA]) group, the center of mass of the H-terminated isoprene group ([ISO]), and the center of mass of the phosphate group (PO_4). Additionally, we have investigated the RDFs associated with the hydrogen atoms of the hydroxy groups within hydroxy-terminated *cis*-1,4-PI chains ($[H]_{OH}$) and the oxygen atoms of these same hydroxy groups ($[O]_{OH}$). These RDFs are denoted as [ISO]−[ISO], $[O]_{OH}$−$[O]_{OH}$, $[O]_{OH}$−$[H]_{OH}$ $[PO_4]$−[DMA], $[O]_{OH}$−[DMA], and [DMA]−[DMA] within ${}_H\text{PI}_H$, ${}_\omega\text{PI}_{\alpha 6}$, and ${}_\omega\text{PI}_{PO_4}$ melt systems. For clarity, it is important to note that the notation [A]−[B] is employed to symbolically represent the arrangement of chemical functional group B around functional group A throughout this study. These RDFs are presented in Figure 5. In $\text{PI}_{0,\text{VI,ph}}$ melt systems, the association between DMA groups exhibits a slightly higher degree compared to that of [ISO]−[ISO]. This observation aligns with our previous research findings.[22,23,25] In the case of PI_{VI}, the position of the first peak in the [O]-[H] RDF in ${}_\omega\text{PI}_{\alpha 6}$ occurs at 0.2 nm, confirming the formation of HBs between the $\alpha 6$ and $\alpha 6$ terminal groups, which facilitates the formation of branch points between hydroxy-terminated PI chains. The intensity of this peak is significantly larger compared to the peaks in [ISO]−[ISO], [O]−[DMA], and [DMA]−[DMA] RDFs. This indicates a strong association of $\alpha 6$ terminal groups in PI chains compared to the ω terminals. In the case of ${}_\omega\text{PI}_{PO_4}$, the $[PO_4]$−$[PO_4]$ RDF peak intensity is notably higher than that of $[PO_4]$−[DMA] and [DMA]−[DMA] RDFs, implying the formation of a strong association between PO_4−PO_4 terminal groups. The number of large-sized polar aggregates between $\alpha 6$ and $\alpha 6$ and PO_4−PO_4 terminals, respectively, in ${}_\omega\text{PI}_{\alpha 6}$ and ${}_\omega\text{PI}_{PO_4}$ melt systems is significantly higher compared to [ISO]−[ISO] in ${}_H\text{PI}_H$. These findings shed light on the solvation structure and molecular associations of terminal groups in the PI systems under study.

The peak intensity of $[PO_4]$−$[PO_4]$ RDF is notably higher compared to $[\alpha 6]$−$[\alpha 6]$ and [ISO]−[ISO] RDFs (see Figure S5). This observation indicates that the $[PO_4]$ terminal groups of PI chains exhibit stronger associations than the hydroxy-terminated PI chains. Notably, we observed narrower RDF peaks between the phosphate terminal groups of phosphate-terminated PI chains, while the first RDF peaks of $\alpha 6$ terminal groups of hydroxy-terminated PI chains are broader. Consequently, the first coordination shell of PO_4 terminals appears to be more ordered than that of $\alpha 6$ terminals. Additionally, the coordination shell of $\alpha 6$ around $\alpha 6$ is more structured compared to that of ISO around ISO. The analysis of running coordination numbers (RCNs) (Figure S6) further supports these findings. Specifically, in the first coordination shell, the number of PO_4 terminal groups around other PO_4 terminals is significantly larger compared to the $\alpha 6$ terminals around other $\alpha 6$ terminals and ISO around ISO terminals. Notably, the value of RCNs in the first coordination shell is highest for PO_4 terminal groups, providing crucial insights into the distinct intermolecular associations and structural order of terminal groups in the PI systems under study.

To investigate the formation of clusters by terminal groups, we employed the single linkage algorithm for association analysis as described in refs 83−85 In the subsequent analysis, we define an "encountering state" of an end-group of a chain with other end-groups that belong to different PI chains. Specifically, when the distance between two end-groups from different chains falls below a threshold distance r_{th} at a specific time step, we identify these end-groups as being in an encountering state. Moreover, if either of the two end-groups is in the encountering state with a different end-group from the other end, we consider the third end-group as being in the encountering state with the first two end-groups. By iteratively applying this procedure to newly added end-groups and stopping when there are no further end-groups to be added, we can determine the size s of the

https://doi.org/10.1021/acspolymersau.4c00019
ACS Polym. Au 2024, 4, 273−288

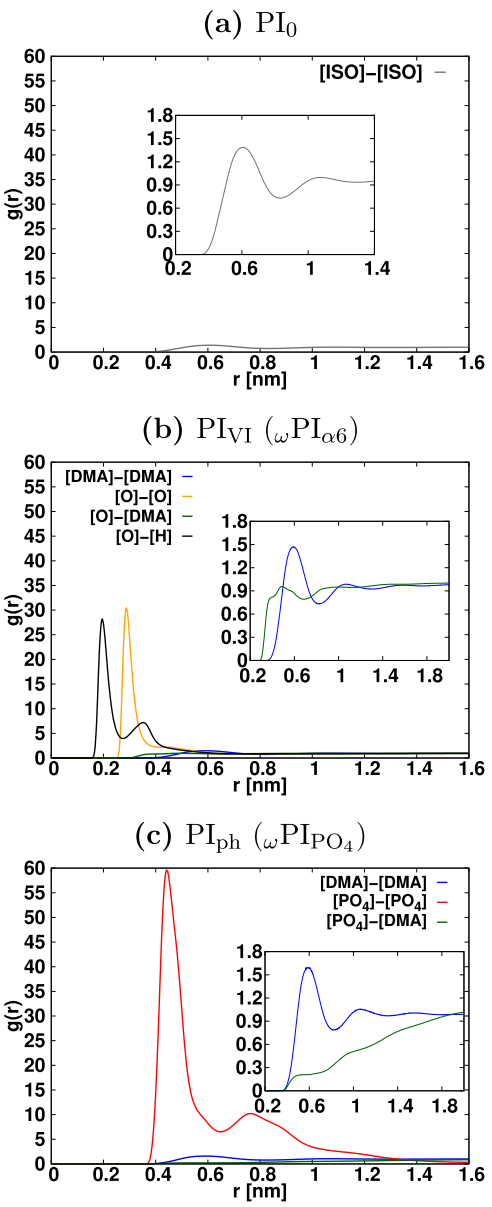

Figure 5. Radial distribution functions (RDFs) depicting the associations between terminal groups in the three types of *cis*-1,4-PI systems. For reference, the RDF of ISO around ISO in the pure PI system (PI_0) is plotted in all graphs, where ″[ISO]″ refers to the center of mass of isoprene residues of terminals. Similarly, ″[DMA]″ denotes the center of mass of dimethyl allyl (dimethyl allyl residue of ω terminal) and ″[PO_4]″ represents the center of mass of the phosphate group. Moreover, [O] and [H] represent oxygen and hydrogen atoms of the hydroxy group in α6-terminals, respectively. In the RDFs, α and β are denoted by the symbols [PO_4], [ISO], [DMA], [O], and [H], and the corresponding associations α–β are color-coded as follows: gray for [ISO]–[ISO], blue for [DMA]–[DMA], red for [PO_4]–[PO_4], dark-green for [PO_4]–[DMA], black for [O]–[H], orange for [O]–[O], and dark-green for [O]–[DMA].

encountering end-groups by counting the number of end-groups involved. Consequently, we evaluate the number n_s of encountering states with size s, thus providing valuable insights into the clustering behavior of terminal groups in the PI system under investigation.

The classification of end-groups in an encountering state is based on whether they contain only a single type of end-group, denoted as α type, in which case the notation $n_s^{\alpha\alpha}$ is employed, or whether they involve two different types of ends, α and β, in which case the notation $n_s^{\alpha\beta}$ is used. To evaluate the number of encountering end-groups of size s, we perform this analysis for K instances during the last 100 ns of the final production run trajectories. Here, K represents the number of frames present in the 100 ns all-atom simulation trajectories, i.e., $n_s^{(\alpha\beta)}(k)$, where k = 1, 2, ..., K = 50,000. Using $n_s^{(\alpha\beta)}(k)$, we define the encountering-event-fraction $f_{enc}^{(\alpha\beta)}(s)$ for a given cluster size s as follows

$$f_{enc}^{(\alpha\beta)}(s) = \frac{1}{M}\frac{1}{K}\sum_{k=1}^{K} n_s^{(\alpha\beta)}(k) \tag{11}$$

where the number of chains in the system is denoted as M. In Figure 6, we present $f_{enc}^{(\alpha\beta)}(s)$ as a function of the encountering-event size s for each melt system. Specifically, $f_{enc}^{(\alpha\beta)}(s = 2)$

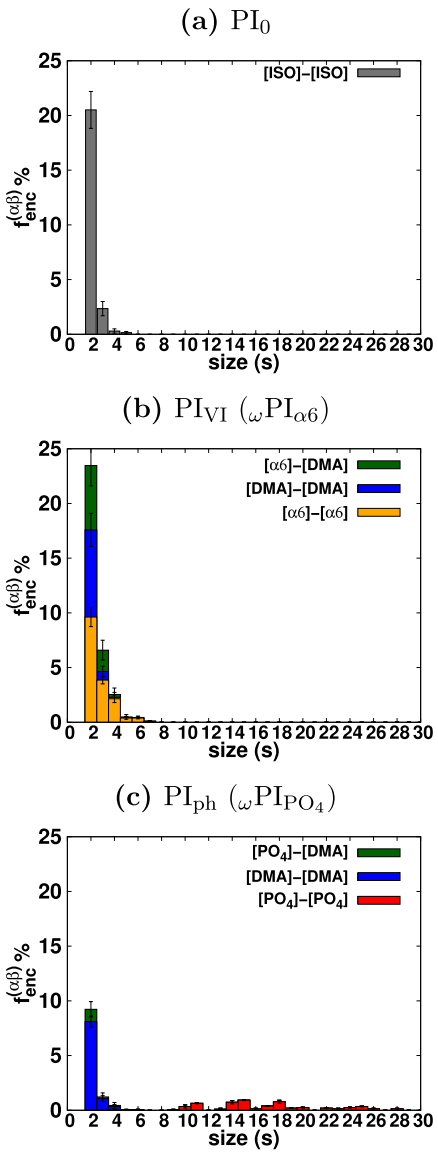

Figure 6. Plot illustrates the fraction of end-group encounters with a cluster size s for the $PI_{0,VI,ph}$ systems. Cut threshold length, r_{th}, is set to 0.6 nm. It is important to note that the sum of the fractions for all cluster sizes, $\sum_{s=1}^{\infty} f_{enc}^{(\alpha\beta)}$ (s = 1), is equal to 1 for each system, ensuring a comprehensive account of all cluster sizes. However, the fractions corresponding to s = 1 are not explicitly shown in the plot.

https://doi.org/10.1021/acspolymersau.4c00019
ACS Polym. Au 2024, 4, 273–288

represents the probability of a terminal group encountering another terminal group, effectively indicating the likelihood of terminal group associations in the form of dimers. If $f_{enc}^{(\alpha\beta)}(s = 2) = 1$, it implies that every terminal group from any chain must be associated with a terminal group from another chain, resulting in 100% of terminal groups forming dimers. However, as the size of the encountering-event increases, the encountering-event-fraction of terminal groups decreases. This suggests that the probability of terminal group associations decreases with the increasing size of the encounter, highlighting the diversity in the sizes and structures of the associations in the PI melt systems. In the case of ${}_{H}PI_{H}$, our observations reveal that the encountering-end-groups predominantly consist of size two, with a few occurrences of size three, and very few instances of size four. However, for ${}_{\omega}PI_{\alpha 6}$, the situation is different. Here, in addition to sizes two and three, encountering-events of larger sizes beyond three is also present due to the strong attractive interactions between $\alpha 6$ and $\alpha 6$ terminal groups, as corroborated by the findings presented in Figure 5. The clusters of size s are evident as $(OH)_{pp}(DMA)_{qq}$ or $(PO_4)_{pp}(DMA)_{qq}$, where pp = 0, 1, 2,···and qq = 0, 1, 2,···with s = pp + qq. In terms of the encountering-event-fractions of size two, the encounter of $[(OH)_2]$ is slightly more frequent than $[(OH)_1(DMA)_1]$ and $[(DMA)_2]$. Moving to size three, $[(OH)_3]$ also dominates over $[(DMA)_3]$, $[(OH)_2(DMA)_1]$, and $[(OH)_1(DMA)_2]$. In the case of size four, $[(OH)_4]$ significantly participates, while the contribution of $[(OH)_1(DMA)_3]$ is minor (the presence of other possibilities like $[(OH)_2(DMA)_2$ is not observed). For size five, only $[(OH)_5]$ is observed, and for size six, only $[(OH)_6]$ exists. The encountering-event-fractions in the ${}_{\omega}PI_{\alpha 6}$ melt systems are more pronounced compared to the ${}_{H}PI_{H}$ system. In the ${}_{\omega}PI_{PO_4}$ system, the encountering-event-fractions of size two are dominated by $[(DMA)_2]$, with the contribution of $[(PO_4)_1(DMA)_1]$ being very small, while $[(PO_4)_2]$ is almost absent. Regarding size three, $[(DMA)_3]$ is more widespread compared to $[(PO_4)_1(DMA)_2]$ and $[(PO_4)_2(DMA)_1]$ while the contribution of $[(PO_4)_3]$ is negligible. For the encountering-event-fractions of size four, $[(DMA)_4]$ predominates over $[(PO_4)_1(DMA)_3]$ (the presence of other possibilities like $[(PO_4)_2(DMA)_2]$ is not observed). For encountering-event-fractions of size larger than four ($4 \leqslant s \leqslant 28$), exclusively $[(PO_4)_{4\text{-to-}28}]$ exists. The observation indicates that the end-groups encounter each other with a certain fraction; however, their stability as branch points or stable clusters remains undetermined. To address this, potentials of mean force (PMFs) have emerged as a widely used approach for assessing the stability of clusters in various research studies.[25,62,86−101] In this study, we compute the PMFs between the terminal groups using the following equation

$$W(r) = -k_B T \log(g(r)) \tag{12}$$

where T is the temperature of the system, k_B is the Boltzmann constant in kJ mol^{-1}/K, and $g(r)$ represents the radial distribution function between the terminal groups. This equation allows us to derive the PMFs, which provide essential insights into the thermodynamic stability and interactions of the terminal groups in the system. We present the PMF between the terminal groups as a function of distance in Figure 7. Each PMF profile exhibits a minimum for contact pairs, which we denote as the contact minimum (CM). In PI_0, we observe a shallow minimum for contact pairs between the two isoprene terminals,

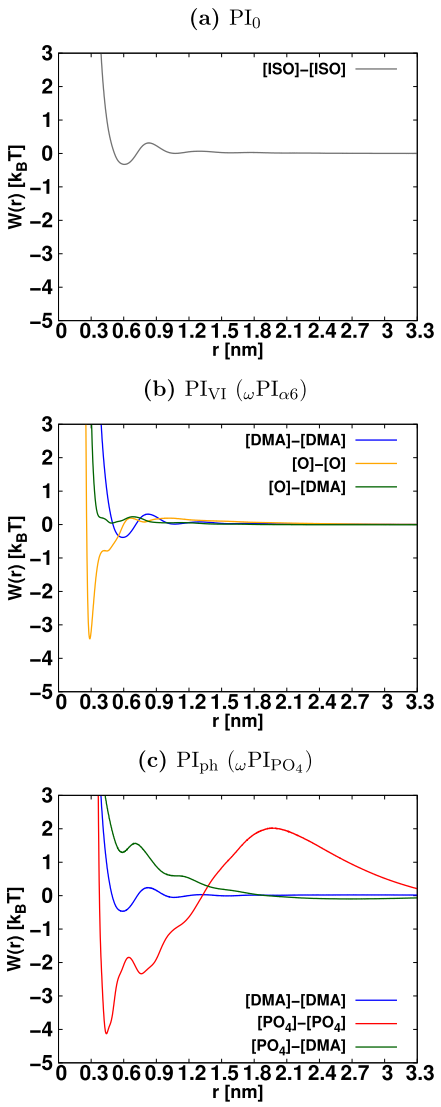

Figure 7. PMF $W(r)$ is calculated by using the equation $W(r) = -k_B T \log(g(r))$, where $g(r)$ is the radial distribution function between the terminal groups. Error bars in each PMFs profile is less than 0.2 $k_B T$.

[ISO]-[ISO], at a distance of 0.6 nm. Similarly, for PI_0 and PI_{VI} melt systems, we perceive a shallow minimum for contact pairs between DMA- and DMA-terminals at 0.6 nm. The interaction free energy of these contact pairs is on the order of thermal energy, indicating that they cannot be considered stable associations. In contrast, for the ${}_{\omega}PI_{\alpha 6}$ system, we observe sharp minima for contact pairs between [OH]−[OH] of $\alpha 6$ terminals, and the stability of this contact pair is substantially higher than the thermal energy. The stability of $\alpha 6$−$\alpha 6$ association is significantly higher than that of [ISO]−[ISO] and [DMA]−[DMA] terminal associations. In the case of the ${}_{\omega}PI_{PO_4}$ system, we notice the formation of a stable contact pair between $[PO_4]$−$[PO_4]$ at a distance of 0.44 nm and between [DMA]−[DMA] at 0.6 nm. The $[PO_4]$−$[PO_4]$ contact pair is more stable than the [DMA]−[DMA] contact pair. For the formation of a stable cluster, the absolute value of the interaction energy $|W|$ at the CM must be significantly greater than the thermal energy. Therefore, we define the criteria for cluster formation as $|W| > 2k_B T$ at the CM. These PMFs provide valuable information about the stability of terminal group

https://doi.org/10.1021/acspolymersau.4c00019
ACS Polym. Au 2024, 4, 273−288

associations and are crucial for understanding the behavior of the terminal groups in the PI systems studied. The dissociation barrier height for the CM of end groups is defined as the free energy difference between the CM and the first maximum of the PMF.[102] Figure 7 clearly shows that the values of dissociation barriers are 10.8 kJ/mol (3.6 k_BT) for the [O]-[O] CM and 17.9 kJ/mol (5.9 k_BT) for the [PO_4]−[PO_4] CM in the $_{\omega}PI_{\alpha 6}$ and $_{\omega}PI_{PO_4}$ melt systems, respectively. These dissociation barrier heights indicate the energy required to break the stable contact pairs, and they offer insights into the stability of terminal group associations in the respective PI systems.

By utilizing the PMF profiles between the terminal groups, we define a stable association between two terminal groups as follows: when the PMF (W) between two terminal groups satisfies the inequality ($|W(r_{CM})| > 2k_BT$), where r_{CM} is the distance at the CM, the two terminal groups are considered to be in a state of stable association and can form a "cluster". To count the number of terminal groups that join a cluster, we apply two criteria: (i) the distance criterion mentioned in eq 11 and (ii) the criterion for stable association ($|W(r_{CM})| > 2k_BT$). The obtained number of clusters with size s is then expressed as $n_s^{(\alpha\beta)}(k;|W(r_{CM})|>2k_BT)$, where α and β represent OH or PO_4 or DMA. The meaning of the superscripts α and β is the same as that used for the number of encountering end groups. For example, $n_s^{(PO_4-DMA)}$ is the number of size s clusters that contain PO_4 and DMA residues of the terminals, and $n_s^{(OH-OH)}$ ($n_s^{(DMA-DMA)}$ or $n_s^{(PO_4-PO_4)}$) is the number of size s clusters composed of only OH (PO_4 or DMA) terminal groups. By using these numbers, we determine the cluster-formation-fraction $f_{cluster}^{(\alpha\beta)}(s)$ with the following equation

$$f_{cluster}^{(\alpha\beta)}(s) = = \frac{1}{M}\frac{1}{K}\sum_{k=1}^{K} n_s^{(\alpha\beta)}(k;|W(r_{CM})|>2k_BT) \quad (13)$$

The cluster-formation-fraction, $f_{cluster}^{(\alpha\beta)}(s)$, is presented in Figure 8. In the case of $_{H}PI_{H}$, the formation of clusters by the terminal groups is entirely absent, while the encountering-events of end-groups are clearly evident, as illustrated in Figure 6. Conversely, for $_{\omega}PI_{\alpha 6}$, clusters of sizes two, three, four, five, and six are observed, with no clusters of size $s \geq 7$ being detected. In the context of $_{\omega}PI_{PO_4}$, clusters of size four, and larger than four are identified. Notably, the associations involving [DMA]−[DMA] and [OH]−[DMA] terminal groups are entirely excluded from cluster formation, aligning with a similar trend reported in our previous work.[25] Furthermore, in the case of $_{\omega}PI_{PO_4}$, cluster-formation-fractions are observed for $4 \leq s \leq 28$, with the associations of [DMA]−[DMA] and [PO_4]−[DMA] terminal groups being fully precluded from cluster formation.

3.4. Survival Time of Terminal Groups in the Coordination Shell

The local rotational and translational mobility of terminal groups is influenced by the duration of time they spend within a specific coordination shell. The survival probability $P(\tau)$ quantifies the fraction of terminal groups that remain within the coordination shell around a given terminal group at time t and continue to be present in the same shell at a later time $t + \tau$. This probability is determined by assessing the likelihood of finding a group of particles remaining in a spherical region with a radius of r_{thrd}, centered at the geometrical center of the selected group.[103,104] The survival probability is calculated using the following equation

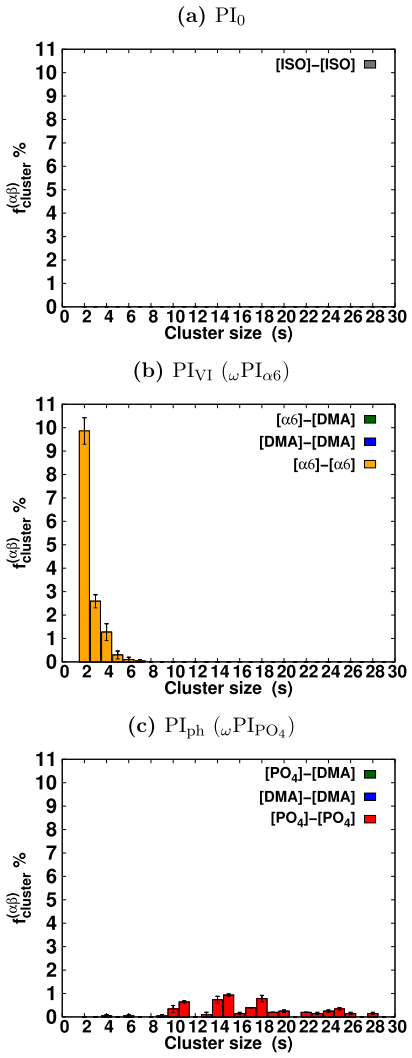

Figure 8. Cluster-formation-fraction as a function of cluster size s in $PI_{0,VI,ph}$ systems. Additional criterion utilizing the magnitude of PMF between terminal groups to determine stable cluster formation. Note that $\sum_{s=1}^{\infty} f_{cluster}^{(\alpha\beta)}(s) = 1$ for each system, and the fractions for $s = 1$ are not shown.

$$P(\tau) = \frac{1}{M_{tot}}\sum_{t=1}^{M_{tot}} \frac{N(t, t+\tau)}{N(t)} \quad (14)$$

where $N(t)$ is the number of terminals in a spherical region with a radius (r_{thrd}) centered at the geometrical center of the selected group assigned to a cluster at time t, $N(t, t + \tau)$ is the number of terminals that continue to stay in the same spherical region from time t to a time $t + \tau$, M_{tot} is the total number of time steps contributing to $P(\tau)$, and τ is the time between the analyzed configurations. The radius r_{thrd} of the selected region for the calculation of $P(\tau)$ for ISO around ISO, DMA around DMA, OH around OH, and PO_4 around PO_4 is chosen based on the RDFs between [ISO]−[ISO], [DMA]−[DMA], [O]−[O], and [PO_4]−[PO_4] (Figure 5). The radius of the first coordination shells of ISO around ISO, DMA around DMA, and O around O is used for the selected regions. MDAnalysis[105] is employed for the calculation of the survival probability. From the investigation of Figure 9, the order of decay of survival probability is $_{H}PI_{H} \ll {}_{\omega}PI_{\alpha 6} \ll {}_{\omega}PI_{PO_4}$. The survival probabilities slowly decay in phosphate-terminated PI chains compared to hydroxy-termi-

https://doi.org/10.1021/acspolymersau.4c00019
ACS Polym. Au 2024, 4, 273−288

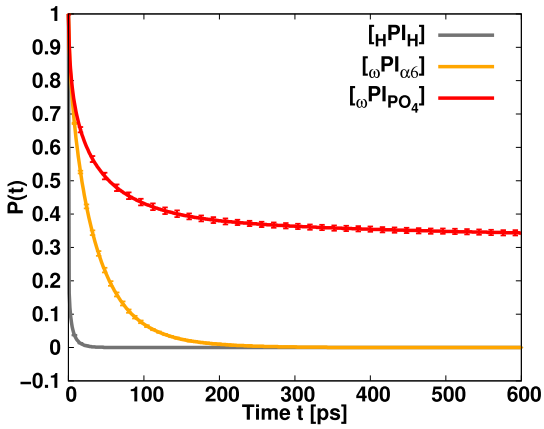

Figure 9. Plot shows the survival probabilities $P(t)$ for terminal groups within the first coordination shell of each terminal group as functions of time duration of t. Survival probabilities were calculated using the last 10 ns of the 1000 ns independent MD simulations. Error bars were calculated using the block-average method. Each survival probability was computed by averaging over the available time windows at given intervals ranging from 1 to 5000 ps.

nated PI. The decay times of the survival probability curves are obtained by fitting them into the Kohlrausch−Williams−Watts (KWW) stretched exponential function, and the estimated values are 6.05 ps $_{H}PI_{H}$, 56.22 ps ($_{\omega}PI_{\alpha 6}$), and 462 ps ($_{\omega}PI_{PO_4}$). The fitted data is shown in Figure S7 of the Supporting Information. These values indicate a much slower exchange rate of terminal groups within the first coordination shell in both phosphorylated and hydroxylated PI chains compared to pure PI. Furthermore, the exchange rate of PO_4 terminal groups within the first coordination shell is much slower compared to hydroxy terminal groups. The decay rates and stretching exponents, along with their error bars, are presented in Table 4.

Table 4. Survival Probability $P(t)$ Is Analyzed Using the Kohlrausch−Williams−Watts Stretched Exponential Function, Enabling the Computation of the Average Relaxation Time τ and the Stretching Exponent β

systems	average relaxation time [ps]	stretching exponents β
$_{H}PI_{H}$	6.05 ± 0.05	0.668 ± 0.001
$_{\omega}PI_{\alpha 6}$	56.22 ± 0.25	0.665 ± 0.002
$_{\omega}PI_{PO_4}$	462 ± 4	0.143 ± 0.001

The relaxation time of phosphate terminal groups interacting with other phosphate terminal groups is considerably longer compared to the relaxation time of hydroxy terminal groups interacting with other hydroxy terminal groups.

3.5. Self-Diffusion Behavior

We analyze the diffusion behavior of individual PI chains in each melt system. The mean square displacement (MSD) of the center of mass of a single PI chain is computed using the last 100 ns of the production-run trajectories

$$\langle (\Delta \boldsymbol{R}_{cm}(t))^2 \rangle \sim t^{\alpha} \tag{15}$$

where $\Delta \boldsymbol{R}_{cm}(t) \equiv \boldsymbol{R}_{cm}(t) - \boldsymbol{R}_{cm}(0)$ and $\langle \Delta \boldsymbol{R}^2_{cm}(t) \rangle$ represent the MSD of the center of mass of a PI chain at time t. The resulting MSD as a function of simulation time is presented in Figure 10. As seen in Figure 10, the MSD does not reach the linear regime yet, but we can see that the self-diffusion of PI with the

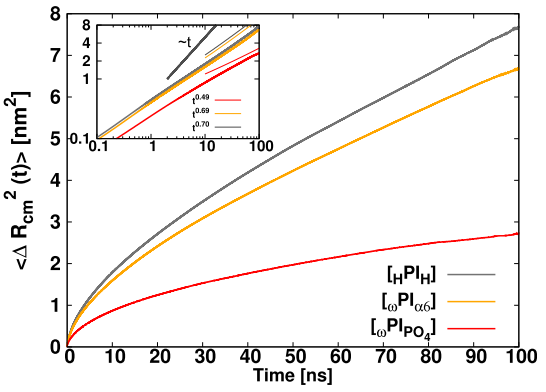

Figure 10. Mean square displacements for the centers of mass of polymer chains in each melt system. Inset stands for the log−log plot of the main graph.

phosphate terminal is suppressed and the diffusion exponent α is substantially smaller than that of $_{H}PI_{H}$ and $_{\omega}PI_{\alpha 6}$. We observed that the center of mass motion of polymer chains is subdiffusive for all three melt systems, i.e., $\langle \Delta \boldsymbol{R}_{cm}{}^2(t) \rangle$ grows as $t^{0.70}$, $t^{0.69}$, and $t^{0.49}$ for $_{H}PI_{H}$, $_{\omega}PI_{\alpha 6}$, and $_{\omega}PI_{PO_4}$, respectively. A similar trend was reported in previous experimental and theoretical studies.[106−110]

We observed that the self-diffusion follows the order: $_{H}PI_{H} > _{\omega}PI_{\alpha 6} \gg _{\omega}PI_{PO_4}$. Thus, the single-chain mobility of the pure-PI system is faster compared to $_{\omega}PI_{\alpha 6}$ and $_{\omega}PI_{PO_4}$ melt systems. The presence of HBs between $\alpha 6-\alpha 6$ and PO_4-PO_4 terminals appears to retard the mobility of hydroxy-terminated and phosphate-terminated PI chains. In particular, we found that the diffusion of $_{\omega}PI_{PO_4}$ molecular chains is significantly slower than that of $_{\omega}PI_{\alpha 6}$ molecular chains.

3.6. Characterization of Polar Physical Junction Points: Insights into Structural Terminal Groups

The investigation into the dynamics of HBs within the polymer melt systems involved the computation of the widely recognized HB time correlation function $C_{HB}(t)$ for pairs of hydrogen-bonded polymer chains denoted as i, j. This correlation function, essential for understanding HB dynamics, follows the definition established in previous studies[111−114]

$$C^{x}_{HB}(t) = \langle \frac{\sum h_{ij}(t_0) h_{ij}(t_0 + t)}{\sum (h_{ij}(t_0))^2} \rangle \tag{16}$$

Here, the dynamic nature of HBs in polymer chains is examined through the variable $h_{ij}(t)$, which quantifies the fulfillment of geometric HB criteria between pairs of polymer chains i and j at time t. The summation covers all potential pairs exhibiting hydrogen-bonding interactions. The angular brackets represent an average over multiple starting times within the trajectory. In the continuous HB correlation framework $C^{c}_{HB}(t)$, it is crucial to highlight that a HB, once disrupted, maintains its broken classification, irrespective of any subsequent reformation. This definition offers insights into the average duration a pair remains bonded, providing the average HB lifetime, denoted as the continuous lifetime τ^{c}_{HB}. In contrast, intermittent HB correlation $C^{I}_{HB}(t)$ explores the persistence probability of a HB formed at $t = 0$, despite multiple breakings and reformations within the time interval $[0, t]$. The corresponding lifetime is referred to as the intermittent lifetime or HB relaxation time τ^{I}_{HB}. We computed both continuous $C^{c}_{HB}(t)$ and intermittent $C^{I}_{HB}(t)$ HB correlation

https://doi.org/10.1021/acspolymersau.4c00019
ACS Polym. Au 2024, 4, 273−288

functions for $\alpha6-\alpha6$ and PO_4-PO_4 utilizing MDAnalysis.[105,115] We conducted an assessment of the continuous $C^c_{HB}(t)$ and intermittent $C^I_{HB}(t)$ HB correlation functions for specific pairs, including $\alpha6-\alpha6$ and PO_4-PO_4, as illustrated in Figure 11.

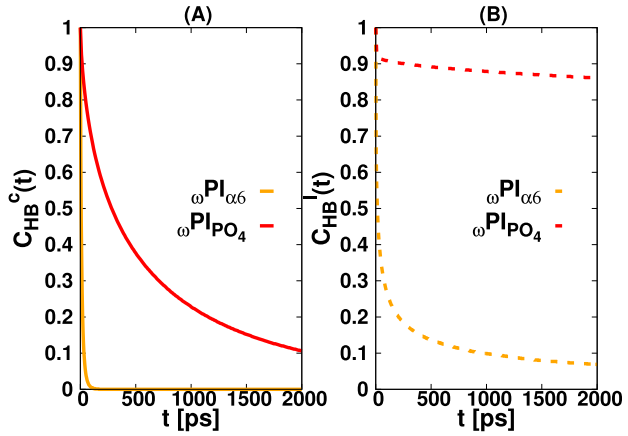

Figure 11. Hydrogen bond correlation functions, the continuous $C_{HB}{}^c(t)$ (A), and intermittent $C_{HB}{}^I(t)$ (B), for pairs $\alpha6-\alpha6$ (orange) and PO_4-PO_4 (red).

Furthermore, the determination of the HB relaxation time τ_{HB} was achieved through fitting the HB autocorrelation functions $C^c_{HB}(t)$ and $C^I_{HB}(t)$ using the KWW stretched exponential function. The resultant values of τ_{HB} and the stretching exponent β_{HB} are documented in Table 5. For the intermittent HB correlation function, we employed the KWW stretched exponential function, specifically expressed as $C^I_{HB}(t) = P^I_{HB} + C^I_{HB}(0)\exp[-(t/\tau^I_{HB})^{\beta^I_{HB}}]$. The estimated values of τ^I_{HB}, stretching exponent β^I_{HB}, and P^I_{HB} are presented in Table 5, offering a detailed characterization of the temporal behavior and persistence of HBs within our studied systems.

Examination of the continuous and intermittent HB lifetimes, as elucidated in Figure 11 and summarized in Table 5, underscores a pronounced distinction between the interactions involving PO_4-PO_4 and $\alpha6-\alpha6$ pairs. The notably protracted continuous lifetime exhibited in PO_4-PO_4 interactions signifies a considerably more robust correlation among hydrogen-bonded ${}_{\omega}PI_{PO_4}$ PI chains in comparison to their ${}_{\omega}PI_{\alpha6}$ counterparts. This observation suggests a higher degree of order and structural organization within the polar physical junctions containing phosphate groups as opposed to those involving OH terminal groups.

4. DISCUSSION AND CONCLUDING REMARKS

We have conducted all-atom MD simulations to investigate three distinct types of *cis*-1,4-PI melt systems featuring various combinations of ω and α' terminal groups. Our analysis encompasses both static and dynamic characteristics of PI chains, including end-to-end distance R_{ee}, radius of gyration R_g, mean square internal distances, end-to-end vector autocorrelation function $C(t)$, average relaxation time τ_{rot}, Rouse mode analysis, survival probability $P(t)$ of terminal groups, HB correlation functions of terminal groups, and self-diffusion behavior of PI chains. The examination of the end-to-end vector autocorrelation function depicted in Figure 2a has unveiled a discernible and intriguing behavior: a sluggish relaxation pattern is evident in PI chains featuring PO_4 terminal groups. This tardy mobility is further substantiated by the reduced translational motion of PI chains in the context of the PO_4-terminated PI melt system, as shown in Figure 10. This behavior strongly implies the likelihood of clustering phenomena between phosphate-terminated PI chains. The Rouse mode analyses (Figure 3) reveal that the intermittent interaction among $\alpha6$-terminals does not induce alterations in Rouse dynamics behavior; nevertheless, it does exert modulation on the time scale of Rouse relaxation. However, the ${}_{\omega}PI_{PO_4}$ melt system showed similar behavior to $1/(p-1/2)^2$, concurrently resulting in a substantial increase in the relaxation time of ${}_{\omega}PI_{PO_4}$ chains. We noted a congruent trend in the observed patterns between the chain relaxation time of the first Rouse mode τ_1 (Table 3) and the rotational relaxation time τ_{rot} (Table of Figure 2). The RDFs between various terminal groups, namely, [ISO]−[ISO], [DMA]−[DMA], $[O]_{OH}-[O]_{OH}$, $[\alpha6]-[\alpha6]$, and $[PO_4]-[PO_4]$ (as illustrated in Figures 5 and S5), offer additional valuable insights into these interactions. For [ISO]−[ISO] and [DMA]−[DMA], the low intensity and broad first RDF peaks indicate a relatively weak association between these groups. Conversely, the presence of a sharper and relatively higher first RDF peak for [DMA]−[DMA] than that of [ISO]−[ISO] suggests a more stable and structured association among ω terminals, especially when compared to the isoprene terminals in the pure PI system PI_0. In the context of ${}_{\omega}PI_{PO_4}$, the most remarkable observation is the significantly higher intensity of the first peak in the $[PO_4]-[PO_4]$ RDFs, in contrast to [ISO]−[ISO] in pure PI, $[O]_{OH}-[O]_{OH}$ in ${}_{\omega}PI_{\alpha6}$, and $\omega-\omega$ in $PI_{0,VI,ph}$ systems. This heightened intensity underscores a much stronger association between PO_4 and PO_4 terminals in the specific context of the ${}_{\omega}PI_{PO_4}$ system. This significant finding is further substantiated by the slower decay of the survival probability for PO_4 around PO_4 terminals, as demonstrated in Figure 9. It is crucial to emphasize that this robust association between phosphate groups is pivotal in the formation of a naturally occurring network, a trend that aligns with prior experimental investigations.[33] This intriguing phenomenon sheds light on the intricate MD and intermolecular interactions in the PI system, especially in the presence of phosphate-terminated chains, which have profound implications for material properties and behavior.

The investigation into the clustering and dynamics of terminal groups within physical junction points was conducted through a comprehensive analysis of three distinct PI melt systems. Our focus centered on assessing the encountering-event-fraction $f^{(\alpha\beta)}_{enc}(s)$ of terminal groups (Figure 6), the PMF between these terminal groups (Figure 7), and the cluster-formation fraction of

Table 5. HB Relaxation Time τ_{HB} and Stretching Exponent β_{HB} for ${}_{\omega}PI_{\alpha6}$ and ${}_{\omega}PI_{\alpha6}$ Melt Systems

	continuous		intermittent		
system	$\tau_{HB}{}^c$ [ps]	$\beta_{HB}{}^c$	$\tau_{HB}{}^I$ [ps]	$\beta_{HB}{}^I$	$P_{HB}{}^I$
${}_{\omega}PI_{\alpha6}$	11.50 ± 0.01	0.798 ± 0.001	32.79 ± 0.18	0.2697 ± 0.0007	0.0170 ± 0.0002
${}_{\omega}PI_{PO_4}$	522.40 ± 0.66	0.610 ± 0.001	371,193 ± 10,720	0.513 ± 0.005	0.0738 ± 0.0007

https://doi.org/10.1021/acspolymersau.4c00019
ACS Polym. Au 2024, 4, 273−288

terminal groups (Figure 8). The outcomes of these analyses provided valuable insights into the unique characteristics exhibited by each melt system. The ${}_{\omega}\mathrm{PI}_{\mathrm{PO}_4}$ melt system demonstrated a prevalence of encountering events of larger sizes, specifically over the range of $(4 \leqslant s \leqslant 28)$, whereas the ${}_{\mathrm{H}}\mathrm{PI}_{\mathrm{H}}$ and ${}_{\omega}\mathrm{PI}_{\alpha 6}$ systems exhibited encountering events of smaller sizes $(2 \leq s \leq 6)$. The structural analysis of the ${}_{\omega}\mathrm{PI}_{\mathrm{PO}_4}$ system further revealed a sharp CM in the PMF $W(r)$ at approximately 0.44 nm. Importantly, the depth of $W(r_{\mathrm{CM}})$ at this CM significantly exceeded the thermal energy (2.99 kJ/mol at 360 K). This observation indicated that the association of PO_4 terminals was notably more stable than the associations of $\alpha 6-\alpha 6$ in $\mathrm{PI}_{\mathrm{VI}}$ and those of $\omega-\omega$ in $\mathrm{PI}_{\mathrm{VI}}$ and $\mathrm{PI}_{\mathrm{ph}}$. This finding was further substantiated by the survival probabilities of terminal groups, reinforcing the enhanced stability of PO_4 associations. Our systematic analysis not only elucidates the distinctive clustering behavior and dynamics within the studied PI melt systems but also highlights the stabilizing effect of phosphate-terminated PI chains, contributing valuable insights to the understanding of molecular interactions in polymer systems.

Our investigation delved into a comprehensive analysis of the cluster-formation-fraction $f_{\mathrm{cluster}}^{(\alpha\beta)}(s)$, enriched by the incorporation of an additional criterion, $(|W(r_{\mathrm{CM}})| > 2k_{\mathrm{B}}T)$. In the ${}_{\omega}\mathrm{PI}_{\mathrm{PO}_4}$ system, a noteworthy revelation unfolded as larger and remarkably stable clusters, spanning the range of four to twenty-eight, emerged. These clusters served as clear indicators of substantially expanded physical junction points within the system. This stands in marked contrast to the ${}_{\omega}\mathrm{PI}_{\alpha 6}$ system, where hydroxy terminal groups orchestrated the establishment of more compact physical junction points, varying in size from two to seven, as depicted in Figure 8. Visual representations capturing the essence of these physical junction points are presented in Figure 12, complemented by Videos S1 and S2 for the ${}_{\omega}\mathrm{PI}_{\alpha 6}$ and ${}_{\omega}\mathrm{PI}_{\mathrm{PO}_4}$ melt systems, respectively. An intriguing alignment with recent experimental findings was observed, underscoring the pivotal role played by phosphate terminal groups in orchestrating the formation of extensive polar aggregates, synonymous with physical junction points, in phosphate-terminated PI chains, as documented by Li et al.[33] In the context of the pure PI melt system, cluster formation exhibited complete suppression due to the feeble association between isoprene-terminal groups.[22−25]

To recapitulate, our investigation probed the impact of ω and α' terminals on both the association of end-terminal groups and the dynamic behavior of PI chains within three distinct melt systems. The presence of a high intensity first RDF peak at 0.2 nm between the $[\mathrm{O}]_{\mathrm{H_2PO_4}}-[\mathrm{H_{(OH)1}}]_{\mathrm{H_2PO_4}}$ and $[\mathrm{O}]_{\mathrm{H_2PO_4}}-[\mathrm{H_{(OH)2}}]_{\mathrm{H_2PO_4}}$ groups confirms the formation of a strong HB between the $\mathrm{H_2PO_4}$ groups (Figure S8). The robust hydrogen-bond interactions observed in $\mathrm{H_2PO_4}-\mathrm{H_2PO_4}$ terminal pairs (Figure S8) facilitated the formation of substantial, stable clusters with sizes greater than 2. These polar aggregates, acting as dynamic cross-linking sites, heightened the cross-linking density, thereby amplifying the mechanical properties of the material. In contrast, the comparatively weaker associations between [ISO]−[ISO] and $\omega-\omega$ terminal pairs precluded the formation of stable clusters, resulting in the absence of steadfast branching points. Consequently, no enduring junctions emerged between ISO−ISO in the case of ${}_{\mathrm{H}}\mathrm{PI}_{\mathrm{H}}$ and between $\omega-\omega$ in the scenarios of ${}_{\omega}\mathrm{PI}_{\alpha 6}$ and ${}_{\omega}\mathrm{PI}_{\mathrm{PO}_4}$. This detailed investigation illuminates the subtle interplay between terminal

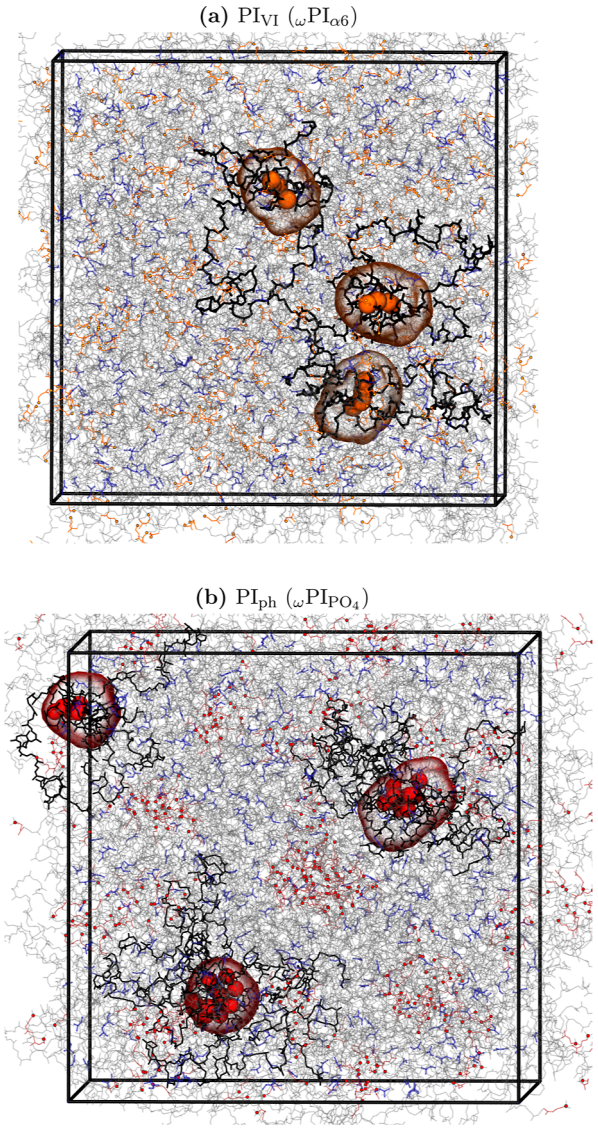

Figure 12. Visualization of physical junction points formed by $\alpha 6$ and PO_4 terminals within $\mathrm{PI_{VI}}$ (a) and $\mathrm{PI_{ph}}$ (b) melt systems, respectively. Dimethyl allyl group of ω terminals is represented in blue, while $\alpha 6$ and PO_4 terminals are color-coded in orange and red, respectively. Depicted orange and red regions are selectively chosen around the atoms within the physical junction points, with a radius of 0.8 nm. Graphical representation employs the quicksurf drawing method with a radius scale of 1.5, a density isovalue of 9.0, and a grid spacing of 2.0. Backbone carbon and hydrogen atoms are illustrated in gray for clarity and context.

associations and cluster stability, offering valuable insights into the mechanical properties of the examined PI melt systems. We have validated the presence of highly stable polar aggregates, formed by robust hydrogen-bond interactions among the phosphate terminals of PI chains. These aggregates hold the potential to be a key factor contributing to the occurrence of SIC observed in NR.

In future research pursuits, we intend to expand our investigation through comprehensive all-atom MD simulations applied to hydroxylated- and phosphorylated-PI melt systems. Our approach will extend beyond traditional rubber constituents to include nonrubber elements such as proteins and phospholipids. This extended exploration seeks to elucidate the intricate interplay between nonrubber components and the

https://doi.org/10.1021/acspolymersau.4c00019
ACS Polym. Au 2024, 4, 273−288

formation of aggregates, whether polar or nonpolar, involving hydroxy- and phosphate-terminal groups of PI chains. The anticipated findings hold the potential to provide deeper insights into the complex molecular interactions governing the exceptional properties of NR, particularly its heightened toughness and the intriguing phenomenon of SIC.

■ ASSOCIATED CONTENT

Supporting Information

The Supporting Information is available free of charge at https://pubs.acs.org/doi/10.1021/acspolymersau.4c00019.

Initial structures of PI melt systems; end-to-end distance (R_{ee}); radius of gyration (R_g); mean square internal distances; time autocorrelation function of normal coordinate of different Rouse modes; RDFs; RCN; and fitted survival probabilities $P(t)$ (PDF)

Formation of polar aggregates between $\alpha 6$ terminals in the ${}_{\omega}PI_{\alpha 6}$ melt system (MP4)

Visual depiction of the formation of polar aggregates between PO_4 terminals in the ${}_{\omega}PI_{PO_4}$ melt system (MP4)

■ AUTHOR INFORMATION

Corresponding Authors

Mayank Dixit − *Graduate School of Engineering, Kyoto University, Kyoto 615-8510, Japan;* orcid.org/0000-0003-2956-6756; Email: dixit@cheme.kyoto-u.ac.jp

Takashi Taniguchi − *Graduate School of Engineering, Kyoto University, Kyoto 615-8510, Japan;* orcid.org/0000-0003-0017-7669; Email: taniguch@cheme.kyoto-u.ac.jp

Complete contact information is available at: https://pubs.acs.org/10.1021/acspolymersau.4c00019

Funding

This work was supported by JST and CREST (grant no. JPMJCR2091), Japan.

Notes

The authors declare no competing financial interest.

■ ACKNOWLEDGMENTS

This work was supported by JST and CREST grant no. JPMJCR2091, Japan. Our heartfelt appreciation extends to Professor Kenji URAYAMA from the Department of Material Chemistry, Graduate School of Engineering, Kyoto University, whose invaluable insights and intellectually stimulating discussions have notably enhanced the outcomes of this research endeavor. We thank Shoma Fujii for providing his code for mean square internal distance and Rouse mode analysis. Furthermore, we extend our gratitude to the Center for Computational Materials Science at the Institute for Materials Research, Tohoku University, for granting us access to the MASAMUNE-IMR platform through project nos. 202112-SCKXX-0017, 202212-SCKXX-0012, and 202312-SCKXX-0004. We also convey our sincere appreciation to the "Joint Usage/Research Center for Interdisciplinary Large-scale Information Infrastructures" and the "High-Performance Computing Infrastructure" in Japan (ProjectID nos. jh210017-MDH, jh220054, jh230061, and jh240063) for their invaluable provision of computational resources. The utilization of computational systems such as Wisteria/BDEC-01, hosted at the Information Technology Center, University of Tokyo, along with Octopus and SQUID located at the Cybermedia Center, Osaka University, has significantly contributed to the successful execution of this research.

■ REFERENCES

(1) Oouchi, M.; Ukawa, J.; Ishii, Y.; Maeda, H. Structural Analysis of the Terminal Groups in Commercial Hevea Natural Rubber by 2D-NMR with DOSY Filters and Multiple-WET Methods Using Ultrahigh-Field NMR. *Biomacromolecules* **2019**, *20*, 1394−1400.

(2) Tarachiwin, L.; Sakdapipanich, J.; Ute, K.; Kitayama, T.; Bamba, T.; Fukusaki, E. I.; Kobayashi, A.; Tanaka, Y. Structural characterization of α-terminal group of natural rubber. 1. Decomposition of branch-points by lipase and phosphatase treatments. *Biomacromolecules* **2005**, *6*, 1851−1857.

(3) Tanaka, Y. Structural characterization of natural polyisoprenes: Solve the mystery of natural rubber based on structural study. *Rubber Chem. Technol.* **2001**, *74*, 355−375.

(4) Cornish, K. Similarities and differences in rubber biochemistry among plant species. *Phytochemistry* **2001**, *57*, 1123−1134.

(5) van Beilen, J. B.; Poirier, Y. Establishment of new crops for the production of natural rubber. *Trends Biotechnol.* **2007**, *25*, 522−529.

(6) Le Cam, J. B.; Toussaint, E. The mechanism of fatigue crack growth in rubbers under severe loading: The effect of stress-induced crystallization. *Macromolecules* **2010**, *43*, 4708−4714.

(7) Toki, S.; Burger, C.; Hsiao, B. S.; Amnuaypornsri, S.; Sakdapipanich, J.; Tanaka, Y. Multi-scaled microstructures in natural rubber characterized by synchrotron X-ray scattering and optical microscopy. *J. Polym. Sci., Part B: Polym. Phys.* **2008**, *46*, 2456−2464.

(8) Gent, A. N.; Kawahara, S.; Zhao, J. Crystallization and Strength of Natural Rubber and Synthetic cis-1,4-Polyisoprene. *Rubber Chem. Technol.* **1998**, *71*, 668−678.

(9) Amnuaypornsri, S.; Toki, S.; Hsiao, B. S.; Sakdapipanich, J. The effects of endlinking network and entanglement to stress-strain relation and strain-induced crystallization of un-vulcanized and vulcanized natural rubber. *Polymer* **2012**, *53*, 3325−3330.

(10) Tang, M.; Zhang, R.; Li, S.; Zeng, J.; Luo, M.; Xu, Y. X.; Huang, G. Towards a Supertough Thermoplastic Polyisoprene Elastomer Based on a Biomimic Strategy. *Angew. Chem., Int. Ed.* **2018**, *57*, 15836−15840.

(11) Payungwong, N.; Inoue, T.; Sakdapipanich, J. A Model Study of the Influence of the Natural Rubber (NR)- Endogenous Gel Fraction on the Rheological Performance of NR Using Synthetic Polyisoprene Rubber (IR) Blends with Different Ratios of Gel. *ACS Appl. Polym. Mater.* **2022**, *4*, 7061−7069.

(12) Wu, J.; Qu, W.; Huang, G.; Wang, S.; Huang, C.; Liu, H. Super-Resolution Fluorescence Imaging of Spatial Organization of Proteins and Lipids in Natural Rubber. *Biomacromolecules* **2017**, *18*, 1705−1712.

(13) Toki, S.; Che, J.; Rong, L. S.; Hsiao, B.; Amnuaypornsri, S.; Nimpaiboon, A.; Sakdapipanich, J. Entanglements and Networks to Strain-Induced Crystallization and Stress-Strain Relations in Natural Rubber and Synthetic Polyisoprene at Various Temperatures. *Macromolecules* **2013**, *46*, 5238−5248.

(14) Kawahara, S.; Matsuura, A.; Kakubo, T.; Nishiyama, N.; Tanaka, Y. Crystallization Behavior of Natural Rubber, Part 3. Effect of Saturated Fatty Acid on Crystallization of cis-1,4-Polyisoprene. *Nippon Gomu Kyokaishi* **1999**, *72*, 413−417.

(15) Kawahara, S.; Tanaka, Y. Plasticization and crystallization of cis-1,4 polyisoprene mixed with methyl linolate. *J. Polym. Sci., Part B: Polym. Phys.* **1995**, *33*, 753−758.

(16) Chen, Q.; Zhang, Z.; Huang, Y.; Zhao, H.; Chen, Z.; Gao, K.; Yue, T.; Zhang, L.; Liu, J. Structure-Mechanics Relation of Natural Rubber: Insights from Molecular Dynamics Simulations. *ACS Appl. Polym. Mater.* **2022**, *4*, 3575−3586.

(17) Xu, L.; Huang, C.; Luo, M.; Qu, W.; Liu, H.; Gu, Z.; Jing, L.; Huang, G.; Zheng, J. A rheological study on non-rubber component networks in natural rubber. *RSC Adv.* **2015**, *5*, 91742−91750.

(18) Zhang, H.; Zhang, L.; Chen, X.; Wang, Y.; Zhao, F.; Luo, M.; Liao, S. The role of non-rubber components on molecular network of natural rubber during accelerated storage. *Polymers* **2020**, *12*, 2880.
(19) Kutsukawa, R.; Imaizumi, R.; Suenaga-Hiromori, M.; Takeshita, K.; Sakai, N.; Misawa, S.; Yamamoto, M.; Yamaguchi, H.; Miyagi-Inoue, Y.; Waki, T.; Kataoka, K.; Nakayama, T.; Yamashita, S.; Takahashi, S. Structure-based engineering of a short-chain cis-prenyltransferase to biosynthesize nonnatural all-cis-polyisoprenoids: molecular mechanisms for primer substrate recognition and ultimate product chain-length determination. *FEBS J.* **2022**, *289*, 4602−4621.
(20) Eng, A.; Kawahara, S.; Tanaka, Y. Trans-isofrene units in natural rubber. *Rubber Chem. Technol.* **1994**, *67*, 159−168.
(21) Gimenez-Dejoz, J.; Tsunoda, K.; Fukushima, Y.; Numata, K. Computational study of the interaction between natural rubber α-terminal groups and l-quebrachitol, one of the major components of natural rubber. *Polym. J. (Tokyo, Jpn.)* **2022**, *54*, 229−233.
(22) Dixit, M.; Taniguchi, T. Role of terminal groups of cis-1,4-polyisoprene in the formation of physical cross-linking in NR — All-atom simulation study. In *Bulletin of the American Physical Society, APS March Meeting 2023*; American Physical Society, 2023; Vol *68*
(23) Dixit, M.; Taniguchi, T. Role of Terminal Groups of cis-1,4-Polyisoprene Chains in the Formation of Physical Junction Points in Natural Rubber. *Biomacromolecules* **2023**, *24*, 3589−3602.
(24) Dixit, M.; Taniguchi, T. Effect of Impurities on the Formation of End-Group Clusters in Natural Rubber: Phenylalanine Dipeptide as an Impurity Protein. *Macromolecules* **2024**, *57*, 2588−2608.
(25) Dixit, M.; Taniguchi, T. Substantial Effect of Terminal Groups in cis-Polyisoprene: A Multiscale Molecular Dynamics Simulation Study. *Macromolecules* **2022**, *55*, 9650−9662.
(26) Tangpakdee, J.; Tanaka, Y. Characterization of sol and gel in hevea natural rubber. *Rubber Chem. Technol.* **1997**, *70*, 707−713.
(27) Tanaka, Y.; Tarachiwin, L. Recent Advances in Structural Characterization of Natural Rubber. *Rubber Chem. Technol.* **2009**, *82*, 283−314.
(28) Kitaura, T.; Kobayashi, M.; Tarachiwin, L.; Kum-ourm, H.; Matsuura, A.; Fushihara, K.; Ute, K. Characterization of Natural Rubber End Groups Using High-Sensitivity NMR. *Macromol. Chem. Phys.* **2018**, *219*, 1700331.
(29) Luo, M. C.; Zeng, J.; Fu, X.; Huang, G.; Wu, J. Toughening diene elastomers by strong hydrogen bond interactions. *Polymer* **2016**, *106*, 21−28.
(30) Hu, B.; Zhou, Y.; Luo, M. C.; Wei, Y. C.; Liu, G. X.; Liao, S.; Zhao, Y. Influence of l -quebrachitol on the properties of centrifuged natural rubber. *e-Polym.* **2021**, *21*, 420−427.
(31) Liu, X.-X.; He, M.-F.; Luo, M.-C.; Wei, Y.-C.; Liao, S. The role of natural rubber endogenous proteins in promoting the formation of vulcanization networks. *e-Polym.* **2022**, *22*, 445−453.
(32) Wei, Y. C.; Liu, G. X.; Zhang, H. F.; Zhao, F.; Luo, M. C.; Liao, S. Non-rubber components tuning mechanical properties of natural rubber from vulcanization kinetics. *Polymer* **2019**, *183*, 121911−121917.
(33) Li, S. Q.; Tang, M. Z.; Huang, C.; Zhang, R.; Huang, G. S.; Xu, Y. X. The Relationship between Pendant Phosphate Groups and Mechanical Properties of Polyisoprene Rubber. *Chin. J. Polym. Sci.* **2021**, *39*, 465−473.
(34) Zhang, R.; Li, S.-Q.; Xu, R.; Wang, C.-C.; Wang, Y.; Huang, G.; Tang, M.; Xu, Y.-X. AGGREGATION BEHAVIORS OF PENDANT PHOSPHORYLCHOLINE GROUPS AND THEIR INFLUENCE ON POLYISOPRENE PROPERTIES. *Rubber Chem. Technol.* **2023**, *96*, 259−275.
(35) Kremer, K.; Grest, G. S. Dynamics of entangled linear polymer melts: A molecular-dynamics simulation. *J. Chem. Phys.* **1990**, *92*, 5057−5086.
(36) Xu, Y.; Hamada, Y.; Taniguchi, T. Multiscale simulations for polymer melt spinning process using Kremer−Grest CG model and continuous fluid mechanics model. *J. Non-Newtonian Fluid Mech.* **2024**, *325*, 105195.
(37) Moe, N. E.; Ediger, M. D. Molecular Dynamics Computer Simulation of Polyisoprene Local Dynamics in Dilute Toluene Solution. *Macromolecules* **1995**, *28*, 2329−2338.
(38) Moe, N. E.; Ediger, M. D. Molecular dynamics computer simulation of local dynamics in polyisoprene melts. *Polymer* **1996**, *37*, 1787−1795.
(39) Moe, N. E.; Ediger, M. D. Computer simulations of polyisoprene local dynamics in vacuum, solution, and the melt: Are conformational transitions always important? *Macromolecules* **1996**, *29*, 5484−5492.
(40) Faller, R.; Reith, D. Properties of poly(isoprene): Model building in the melt and in solution. *Macromolecules* **2003**, *36*, 5406−5414.
(41) Egami, T. Local structure and dynamics of ferroelectric solids. *Struct. Bonding (Berlin)* **2007**, *124*, 69−88.
(42) Diani, J.; Gall, K. Molecular dynamics simulations of the shape-memory behaviour of polyisoprene. *Smart Mater. Struct.* **2007**, *16*, 1575−1583.
(43) Maple, J. R.; Dinur, U.; Hagler, A. T. Derivation of force fields for molecular mechanics and dynamics from ab initio energy surfaces. *Proc. Natl. Acad. Sci. U.S.A.* **1988**, *85*, 5350−5354.
(44) Deutsch, H. P.; Binder, K. Interdiffusion and self-diffusion in polymer mixtures: A Monte Carlo study. *J. Chem. Phys.* **1991**, *94*, 2294−2304.
(45) Ercolessi, F.; Adams, J. B. Interatomic Potentials from First-Principles Calculations: The Force-Matching Method. *Europhys. Lett.* **1994**, *26*, 583−588.
(46) Tschöp, W.; Kremer, K.; Batoulis, J.; Bürger, T.; Hahn, O. Simulation of polymer melts. I. Coarse-graining procedure for polycarbonates. *Acta Polym.* **1998**, *49*, 61−74.
(47) Lyubartsev, A. P.; Laaksonen, A. Calculation of effective interaction potentials from radial distribution functions: A reverse Monte Carlo approach. *Phys. Rev. E* **1995**, *52*, 3730−3737.
(48) Meyer, H.; Biermann, O.; Faller, R.; Reith, D.; Müller-Plathe, F. Coarse graining of nonbonded inter-particle potentials using automatic simplex optimization to fit structural properties. *J. Chem. Phys.* **2000**, *113*, 6264−6275.
(49) Mullinax, J. W.; Noid, W. G. Reference state for the generalized Yvon-Born-Green theory: Application for coarse-grained model of hydrophobic hydration. *J. Chem. Phys.* **2010**, *133*, 124107.
(50) Shell, M. S. The relative entropy is fundamental to multiscale and inverse thermodynamic problems. *J. Chem. Phys.* **2008**, *129*, 144108.
(51) Izvekov, S.; Voth, G. A. A multiscale coarse-graining method for biomolecular systems. *J. Phys. Chem. B* **2005**, *109*, 2469−2473.
(52) Uddin, M. S.; Ju, J. Multiscale modeling of a natural rubber: Bridging a coarse-grained molecular model to the rubber network theory. *Polymer* **2016**, *101*, 34−47.
(53) Li, Y.; Kröger, M.; Liu, W. K. Primitive chain network study on uncrosslinked and crosslinked cis-polyisoprene polymers. *Polymer* **2011**, *52*, 5867−5878.
(54) Kawaguchi, N.; Okubo, K.; Aida, K. Molecular cloning and expression of corticotropin-releasing hormone and urotensin I in the medaka, Oryzias latipes. *Fish. Sci.* **2002**, *68*, 1281−1282.
(55) Pandey, Y. N.; Brayton, A.; Burkhart, C.; Papakonstantopoulos, G. J.; Doxastakis, M. Multiscale modeling of polyisoprene on graphite. *J. Chem. Phys.* **2014**, *140*, 054908.
(56) Moe, N. E.; Ediger, M. D. Calculation of the coherent dynamic structure factor of polyisoprene from molecular dynamics simulations. *Phys. Rev. E: Stat. Phys., Plasmas, Fluids, Relat. Interdiscip. Top.* **1999**, *59*, 623−630.
(57) Li, Y.; Mattice, W. L. Atom-Based Modeling of Amorphous 1,4-cis-Polybutadiene. *Macromolecules* **1992**, *25*, 4942−4947.
(58) Ohkuma, T.; Kremer, K. A composition transferable and time-scale consistent coarse-grained model for cis-polyisoprene and vinyl-polybutadiene oligomeric blends. *JPhys Mater.* **2020**, *3*, 034007.
(59) Ohkuma, T.; Kremer, K. Comparison of two coarse-grained models of cis-polyisoprene with and without pressure correction. *Polymer* **2017**, *130*, 88−101.
(60) Shukla, R.; Ray, D.; Sarkar, K.; Kumar Dixit, M.; Prasad Bhattacharyya, S. Flying onto global minima on potential energy

surfaces: A swarm intelligence guided route to molecular electronic structure. *Int. J. Quantum Chem.* **2016**, *117*, No. e25328.
(61) Ghosh, S.; Dixit, M.; Bhattacharyya, S.; Tembe, B. Franck-condon factors for diatomics: Insights and analysis using the Fourier Grid Hamiltonian method. *J. Chem. Educ.* **2013**, *90*, 1463−1471.
(62) Siddique, A.; Dixit, M.; Tembe, B. Molecular dynamics simulations of Ca^{2+} Cl^{-} ion pair in polar mixtures of acetone and water: Solvation and dynamical studies. *Chem. Phys. Lett.* **2016**, *662*, 306−316.
(63) Choi, Y. K.; Park, S. J.; Park, S.; Kim, S.; Kern, N. R.; Lee, J.; Im, W. CHARMM-GUI Polymer Builder for Modeling and Simulation of Synthetic Polymers. *J. Chem. Theory Comput.* **2021**, *17*, 2431−2443.
(64) Lehman, N.; Tuljittraporn, A.; Songtipya, L.; Uthaipan, N.; Sengloyluan, K.; Johns, J.; Nakaramontri, Y.; Kalkornsurapranee, E. Influence of Non-Rubber Components on the Properties of Unvulcanized Natural Rubber from Different Clones. *Polymers* **2022**, *14*, 1759.
(65) Nun-anan, P.; Wisunthorn, S.; Pichaiyut, S.; Nathaworn, C. D.; Nakason, C. Influence of nonrubber components on properties of unvulcanized natural rubber. *Polym. Adv. Technol.* **2020**, *31*, 44−59.
(66) Nun-anan, P.; Wisunthorn, S.; Pichaiyut, S.; Vennemann, N.; Nakason, C. Novel approach to determine non-rubber content in Hevea brasiliensis: Influence of clone variation on properties of unvulcanized natural rubber. *Ind. Crops Prod.* **2018**, *118*, 38−47.
(67) Mooibroek, H.; Cornish, K. Alternative sources of natural rubber. *Appl. Microbiol. Biotechnol.* **2000**, *53*, 355−365.
(68) Lockwood, G. GAS CHROMATOGRAPHY | Terpenoids. *Reference Module in Chemistry, Molecular Sciences and Chemical Engineering* **2013**.
(69) Abraham, M. J.; Murtola, T.; Schulz, R.; Páll, S.; Smith, J. C.; Hess, B.; Lindahl, E. Gromacs: High performance molecular simulations through multi-level parallelism from laptops to supercomputers. *SoftwareX* **2015**, *1−2*, 19−25.
(70) Allouche, A.-r. Gabedit—A graphical user interface for computational chemistry softwares. *J. Comput. Chem.* **2011**, *32*, 174−182.
(71) Vanommeslaeghe, K.; Hatcher, E.; Acharya, C.; Kundu, S.; Zhong, S.; Shim, J.; Darian, E.; Guvench, O.; Lopes, P.; Vorobyov, I.; Mackerell, A. D. CHARMM general force field: A force field for drug-like molecules compatible with the CHARMM all-atom additive biological force fields. *J. Comput. Chem.* **2010**, *31*, 671−690.
(72) Parrinello, M.; Rahman, A. Polymorphic transitions in single crystals: A new molecular dynamics method. *J. Appl. Phys.* **1981**, *52*, 7182−7190.
(73) Hess, B.; Bekker, H.; Berendsen, H. J.; Fraaije, J. G. LINCS: A Linear Constraint Solver for molecular simulations. *J. Comput. Chem.* **1997**, *18*, 1463−1472.
(74) Darden, T.; York, D.; Pedersen, L. Particle mesh Ewald: An $N\cdot\log(N)$ method for Ewald sums in large systems. *J. Chem. Phys.* **1993**, *98*, 10089−10092.
(75) Fetters, L.; Lohse, D.; Colby, R. *Physical Properties of Polymers Handbook*; Springer, 2007; pp 447−454.
(76) Williams, G.; Watts, D. C. Non-symmetrical dielectric relaxation behaviour arising from a simple empirical decay function. *Trans. Faraday Soc.* **1970**, *66*, 80−85.
(77) Doi, M.; Edwards, S.; Edwards, S. *The Theory of Polymer Dynamics; International Series of Monographs on Physics*; Clarendon Press, 1988; .
(78) Verdier, P. H. Monte carlo studies of lattice-model polymer chains. i. correlation functions in the statistical-bead model. *J. Chem. Phys.* **1966**, *45*, 2118−2121.
(79) Kopf, A.; Dünweg, B.; Paul, W. Dynamics of polymer "isotope" mixtures: Molecular dynamics simulation and Rouse model analysis. *J. Chem. Phys.* **1997**, *107*, 6945−6955.
(80) Harmandaris, V. A.; Mavrantzas, V. G.; Theodorou, D. N. Atomistic molecular dynamics simulation of polydisperse linear polyethylene melts. *Macromolecules* **1998**, *31*, 7934−7943.
(81) Tsolou, G.; Harmandaris, V. A.; Mavrantzas, V. G. Molecular dynamics simulation of temperature and pressure effects on the intermediate length scale dynamics and zero shear rate viscosity of cis-1,4-polybutadiene: Rouse mode analysis and dynamic structure factor spectra. *J. Non-Newtonian Fluid Mech.* **2008**, *152*, 184−194.
(82) Vandoolaeghe, W. L.; Terentjev, E. M. Constrained Rouse model of rubber viscoelasticity. *J. Chem. Phys.* **2005**, *123*, 034902.
(83) Janosi, L.; Li, Z.; Hancock, J. F.; Gorfe, A. A. Organization, dynamics, and segregation of Ras nanoclusters in membrane domains. *Proc. Natl. Acad. Sci. U.S.A.* **2012**, *109*, 8097−8102.
(84) Li, Z.; Dormidontova, E. E. Kinetics of diblock copolymer micellization by dissipative particle dynamics. *Macromolecules* **2010**, *43*, 3521−3531.
(85) Marrink, S. J.; Tieleman, D. P.; Mark, A. E. Molecular dynamics simulation of the kinetics of spontaneous micelle formation. *J. Phys. Chem. B* **2000**, *104*, 12165−12173.
(86) Dixit, M.; Chatterjee, A.; Tembe, B. Salting-out of methane in the aqueous solutions of urea and sarcosine. *J. Chem. Sci.* **2016**, *128*, 599−612.
(87) Dixit, M.; Hajari, T.; Tembe, B. The effect of urea and taurine osmolytes on hydrophobic association and solvation of methane and neopentane molecules. *J. Mol. Liq.* **2016**, *223*, 660−671.
(88) Dixit, M.; Hajari, T.; Tembe, B. Solvation structures of sodium halides in dimethyl sulfoxide (DMSO) − − methanol (MeOH) mixtures. *Mol. Simul.* **2017**, *43*, 154−168.
(89) Dixit, M.; Hajari, T.; Meti, M. D.; Srivastava, S.; Srivastava, A.; Daniel, J. Ionic Pairing and Selective Solvation of Butylmethylimidazolium Chloride Ion Pairs in DMSO−Water Mixtures: A Comprehensive Examination via Molecular Dynamics Simulations and Potentials of Mean Force Analysis. *J. Phys. Chem. B* **2024**, *128*, 2168−2180.
(90) Dixit, M.; Siddique, A.; Tembe, B. Salting-Out of Methane in the Aqueous Solutions of Urea and Glycine-Betaine. *J. Phys. Chem. B* **2015**, *119*, 10941−10953.
(91) Sarkar, A.; Dixit, M.; Tembe, B. Solvation structures of lithium halides in methanol-water mixtures. *Chem. Phys.* **2015**, *447*, 76−85.
(92) Meti, M.; Dixit, M.; Hajari, T.; Tembe, B. Ion pairing and preferential solvation of butylmethylimidazolium chloride ion pair in water-ethanol mixtures by using molecular dynamics simulations. *Chem. Phys. Lett.* **2019**, *720*, 107−112.
(93) Hajari, T.; Dixit, M.; Yadav, H. Hydrophobic association and solvation of neopentane in urea, TMAO and urea-TMAO solutions. *Phys. Chem. Chem. Phys.* **2022**, *24*, 6941−6957.
(94) Ghosh, S.; Dixit, M.; Chakrabarti, R. Thermodynamics of site-specific small molecular ion interactions with DNA duplex: A molecular dynamics study. *Mol. Simul.* **2016**, *42*, 715−724.
(95) Meti, M.; Dixit, M.; Tembe, B. Salting-in of neopentane in the aqueous solutions of urea and glycine-betaine. *Mol. Simul.* **2018**, *44*, 677−687.
(96) Kumar, A.; Mahato, J.; Dixit, M.; Patwari, G. Progressive Hydrophobicity of Fluorobenzenes. *J. Phys. Chem. B* **2019**, *123*, 10083−10088.
(97) Chatterjee, A.; Dixit, M.; Tembe, B. Solvation Structures and Dynamics of the Magnesium Chloride (Mg^{2+} - Cl^{-}) Ion Pair in Water-Ethanol Mixtures. *J. Phys. Chem. A* **2013**, *117*, 8703−8709.
(98) Dixit, M.; Tembe, B. Potentials of mean force of sodium chloride ion pair in dimethyl sulfoxide-methanol mixtures. *J. Mol. Liq.* **2013**, *178*, 78−83.
(99) Siddique, A.; Dixit, M.; Tembe, B. Solvation structure and dynamics of potassium chloride ion pair in dimethyl sulfoxide-water mixtures. *J. Mol. Liq.* **2013**, *188*, 5−12.
(100) Jain, A.; Dixit, M.; Tembe, B. Preferential solvation and association constants of 2- Exo and 2- Endo norbornyl chlorides in water-acetone mixtures. *Mol. Simul.* **2014**, *40*, 987−995.
(101) Dixit, M.; Lazaridis, T. Free energy of hydrophilic and hydrophobic pores in lipid bilayers by free energy perturbation of a restraint. *J. Chem. Phys.* **2020**, *153*, 054101.
(102) Justice, M. C.; Justice, J. C. Ionic interactions in solutions. I. The association concepts and the McMillan-Mayer theory. *J. Solution Chem.* **1976**, *5*, 543−561.

https://doi.org/10.1021/acspolymersau.4c00019
ACS Polym. Au 2024, 4, 273−288

(103) Liu, P.; Harder, E.; Berne, B. J. On the calculation of diffusion coefficients in confined fluids and interfaces with an application to the liquid-vapor interface of water. *J. Phys. Chem. B* **2004**, *108*, 6595−6602.
(104) Araya-Secchi, R.; Perez-Acle, T.; Kang, S. G.; Huynh, T.; Bernardin, A.; Escalona, Y.; Garate, J. A.; Martínez, A.; García, I.; Sáez, J.; Zhou, R. Characterization of a novel water pocket inside the human Cx26 hemichannel structure. *Biophys. J.* **2014**, *107*, 599−612.
(105) Gowers, R.; Linke, M.; Barnoud, J.; Reddy, T.; Melo, M.; Seyler, S.; Domański, J.; Dotson, D.; Buchoux, S.; Kenney, I.; Beckstein, O. MDAnalysis: A Python Package for the Rapid Analysis of Molecular Dynamics Simulations. In *Proceedings of the 15th Python in Science Conference*, 2016; pp 98−105.
(106) Paul, W.; Smith, G. D.; Yoon, D. Y. Static and dynamic properties of a n-C100H202 melt from molecular dynamics simulations. *Macromolecules* **1997**, *30*, 7772−7780.
(107) Paul, W.; Smith, G. D.; Yoon, D. Y.; Farago, B.; Rathgeber, S.; Zirkel, A.; Willner, L.; Richter, D. Chain motion in an unentangled polyethylene melt: A critical test of the rouse model by molecular dynamics simulations and neutron spin echo spectroscopy. *Phys. Rev. Lett.* **1998**, *80*, 2346−2349.
(108) Paul, W.; Binder, K.; Heermann, D. W.; Kremer, K. Dynamics of polymer solutions and melts. Reptation predictions and scaling of relaxation times. *J. Chem. Phys.* **1991**, *95*, 7726−7740.
(109) Smith, G. D.; Paul, W. United Atom Force Field for Molecular Dynamics Simulations of 1,4-Polybutadiene Based on Quantum Chemistry Calculations on Model Molecules. *J. Phys. Chem. A* **1998**, *102*, 1200−1208.
(110) Smith, G. D.; Paul, W.; Monkenbusch, M.; Richter, D. On the non-Gaussianity of chain motion in unentangled polymer melts. *J. Chem. Phys.* **2001**, *114*, 4285−4288.
(111) Rapaport, D. C. Hydrogen bonds in water network organization and lifetimes. *Mol. Phys.* **1983**, *50*, 1151−1162.
(112) Skarmoutsos, I.; Guardia, E.; Samios, J. Hydrogen bond, electron donor-acceptor dimer, and residence dynamics in supercritical CO2-ethanol mixtures and the effect of hydrogen bonding on single reorientational and translational dynamics: A molecular dynamics simulation study. *J. Chem. Phys.* **2010**, *133*, 014504.
(113) Skarmoutsos, I.; Guardia, E. Local Structural Effects and Related Dynamics in Supercritical Ethanol. 2. Hydrogen-Bonding Network and Its Effect on Single Reorientational Dynamics. *J. Phys. Chem. B* **2009**, *113*, 8898−8910.
(114) Stillinger, F. H. *Advances in Chemical Physics*; Wiley, 1975; Vol. *31*.
(115) Gowers, R. J.; Carbone, P. A multiscale approach to model hydrogen bonding: The case of polyamide. *J. Chem. Phys.* **2015**, *142*, 224907.

https://doi.org/10.1021/acspolymersau.4c00019
ACS Polym. Au 2024, 4, 273−288